

Mathematical Modelling and Simulation of a PWM Inverter Controlled Brushless Motor Drive System from Physical Principles for Electric Vehicle Propulsion Applications

Richard A. Guinee
*Cork Institute of Technology,
Ireland*

1. Introduction

High performance electric motor drive systems are central to modern electric vehicle propulsion systems (Emadi et al. , 2003) and are also widely used in industrial automation (Dote, 1990) in such scenarios as numerical control (NC) machine tools and robotics. The benefits accruing from the application of such drives are precision control of torque, speed and position which promote superior electric vehicle dynamical performance (Miller, 2010) with reduced greenhouse carbon gaseous emissions resulting in increased overall automotive efficiencies. These electric motor drive attributes also contribute to enhanced productivity in the industrial sector with high quality manufactured products. These benefits arise from the fusion of modern adaptive control techniques (El Sarkawi, 1991) with advances in motor technology, such as permanent magnet brushless motors, and high speed solid-state switching converters which constitute the three essential ingredients of a high performance embedded drive system. The controllers of these machine drives are adaptively tuned to meet the essential requirements of system robustness and high tracking performance without overstressing the hardware components (Demerdash et al, 1980; Dawson et al, 1998). Conventional d.c. motors were traditionally used in adjustable speed drive (ASD) applications because torque and flux control were easily achieved by the respective adjustment of the armature and field currents in separately excited systems where fast response was a requirement with high performance at very low speeds (Vas, 1998). These dc motors suffer from the drawback of a mechanical commutator assembly fitted with brushes for electrical continuity of the rotor mounted armature coil which increases the shaft inertia and reduces speed of response. Furthermore they require periodic maintenance because of brush wear which limits motor life and the effectiveness of the commutator for high speed applications due to arcing and heating with high current carrying capacity (Murugesan, 1981).

Brushless motor drive (BLMD) systems, which incorporate wide bandwidth speed and torque control loops, are extensively used in modern high performance EV and industrial motive power applications as control kernels instead of conventional dc motors. Typical high performance servodrive applications (Kuo, 1978; Electrocraft Corp, 1980) which require high torque and precision control, include chemical processing, CNC machines, supervised

actuation in aerospace and guided robotic manipulations (Asada et al, 1987). This is due largely to the high torque-to-weight ratio and compactness of permanent magnet (PM) drives and the virtually maintenance free operation of brushless motors in inaccessible locations when compared to conventional DC motors. These PM machines are also used for electricity generation (Spooner et al, 1996) and electric vehicle propulsion (Friedrick et al, 1998) because of their higher power factor and efficiency. Furthermore the reported annual World growth rate of 25% per annum (Mohan, 1998) in the demand for of all types of adjustable speed drives guarantees an increased stable market share for PM motors over conventional dc motors in high performance EV and industrial drive applications. This growth is propelled by the need for energy conservation and by technical advances in Power Electronics and DSP controllers.

The use of low inertia and high energy Samarium Cobalt-rare earth magnetic materials in PM rotor construction (Noodleman, 1975), which produces a fixed magnetic field of high coercivity, results in significant advantages over dc machines by virtue of the elimination of mechanical commutation and brush arching radio frequency interference (RFI). These benefits include the replacement of the classical rotor armature winding and brush assembly which means less wear and simpler machine construction. Consequently the PM rotor assembly is light and has a relatively small diameter which results in a low rotor inertia. The rotating PM structure is rugged and resistant to both mechanical and thermal shock at high EV speeds. Furthermore high standstill/peak torque is attainable due to the absence of brushes and high air-gap flux density. When this high torque feature is coupled with the low rotor inertia extremely high dynamic performance is produced for EV propulsion due to rapid acceleration and deceleration over short time spans. The reduction in weight and volume for a given horsepower rating results in the greatest possible motor power-to-mass ratio with a wide operating speed range and lower response times thus makes PM motors more suitable for variable speed applications. Greater heat dissipation is afforded by the stationary machine housing, which provides large surface area and improved heat transfer characteristics, as the bulk of the losses occur in the stator windings (Murugesan, 1981). The operating temperature of the rotor is low since the permanent magnets do not generate heat internally and consequently the lifetime of the motor shaft bearings is increased.

There are three basic types of PM motor available depending on the magnetic alignment and mounting on the rotor frame. The permanent magnet synchronous motor (PMSM) behaves like a uniform gap machine with rotor surface-mounted magnets. This magnetic configuration results in equal direct d -axis and quadrature q -axis synchronous inductance components and consequently only a magnetic torque is produced. If the PM magnets are inset into the rotor surface then salient pole machine behaviour results with unequal d and q inductances in which both magnetic and reluctance torque are produced. A PMSM with buried magnets in the rotor frame also produces both magnetic and reluctance torque. There are three types of PM machine with buried magnetic field orientation which include radial, axial and inclined interior rotor magnet placement (Boldea, 1996). Brushless motor drives (Hendershot et al, 1994; Basak, 1996) are categorized into two main groups based on (a) current source inverter fed BLMD systems with a trapezoidal flux distribution (Persson, 1976) and (b) machines fed with sinusoidal stator currents with a sinusoidal air-gap flux distribution (Leu et al, 1989).

BLMD systems also have a number of significant operational features in addition to the above stated advantages, that are key requirements in high performance embedded drive applications, by comparison with conventional dc motor implementations which can be summarized as follows:

- i. DC motor emulation is made possible through electronic commutation of the PM synchronous motor three phase stator winding in accordance with sensed rotor position (Demerdash et al, 1980; Dohmeki, 1985).
- ii. In addition to (i) pulse-width modulation (PWM) (Tal, 1976), which is generally used in brushless motor inverter control as the preferred method of power dispatch as a form of class S amplification (Kraus et al, 1980), provides a wide range of continuous power output. This is much more energy efficient than its linear class A counterpart in servo-amplifier operation.
- iii. BLMD systems have a linear torque-speed characteristic (Murugesan, *ibid*) because of the high PM coercivity which ensures fixed magnetic flux at all loads. If the PMSM is fed by a current controlled voltage source inverter (VSI) then the instantaneous currents in the stator winding are forced to track the reference values determined by the torque command or speed reference.
- iv. Direct torque drive capability with higher coupling stiffness and smooth torque operation at very low shaft speeds, without torque ripple, is feasible without gears resulting in better positional accuracy in EVs.

The decision as to the eventual choice of a particular drive type ultimately depends on the embedded drive system application in terms of operational drive performance specification, accessible space available to house the physical size of the motor, and to meet drive ventilation requirements for dissipated motor heating. The decision will also be influenced by operational efficiency consideration of embedded drive power and torque delivery and the required level of accuracy needed for the application controlled variable be it position, velocity or acceleration.

Consideration of the benefits of using PM motors in high performance electric vehicle (EV) propulsion illustrates the need for an accurate model description (Leu et al, *ibid*) of the complete BLMD system based on internal physical structures for the purpose of simulation and parameter identification of the nonlinear drive electrodynamics. This is necessary for behavioural simulation accuracy and performance related prediction in feasibility studies where new embedded motor drives in EV systems are proposed. Furthermore an accurate discrete time BLMD simulation model is an essential prerequisite in EV optimal controller design where system identification is an implicit feature (Ljung, 1991, 1992). Concurrent with model development is the requirement for an efficient optimization search strategy in parameter space for accurate extraction of the system dynamics. Two important interrelated areas where system modelling with parameter identification plays a key role in controller design and performance for industrial automation include PID auto-tuning and adaptive control. PID auto-tuning (Astrom et al, 1989) of wide bandwidth current loops in torque controlled motor drives make it possible to speed EV commissioning and facilitate control optimization through regular retuning by comparison with the manual application of the empirical Ziegler -Nichols tuning rule using transient step response data. Typical methods employed in auto-tuner PID controllers (Astrom et al, 1988, 1989; Hang et al, 1991) are pattern recognition and relay feedback, which is the simplest. Implementation of the self oscillating relay feedback method in the current loops of a brushless motor drive is difficult and complex because of internal system structure and connectivity with three phase current (3 Φ) commutation. Proper selection of the PID term parameters in PID controller setup, from dynamical parameter identification, is necessary to avoid significant overshoot and oscillations in precision control applications (Sarkawi, *ibid*). This is dependent to a great

extent on an accurate physical model of the nonlinear electromechanical system (Krause et al, 1989) including the PWM controlled inverter with substantial transistor turnon delay as this reflects the standard closed loop drive system configuration and complexity during normal online operation. Motor parameter identification, based on input/output (I/O) data records, enable suitable PID settings to be chosen and subsequent overall system performance can be validated from model simulation trial runs with further retuning if necessary. Auto-tuning can also be used for pre-tuning more complex adaptive structures such as self tuning (STR) and model reference adaptive systems (MRAS). The method of identification of EV motor drive shaft load inertia and viscous damping parameters, based on the chosen physical model of BLMD operation, is one of constrained optimization in such circumstances. This is a minimization search procedure manifested in the reduction of an objective function, generally based on the least mean squares error (MSE) criterion (Soderstrom, 1989) as a penalty cost measure, in accordance with the optimal adjustment of the model parameter set. The objective function is expressed as the mean squared difference, for sampled data time records, between actual drive chosen output (o/p) as the target function and its model equivalent. This quadratic error performance index, which provides a measure of the goodness of fit of the model simulation and should ideally have a paraboloidal landscape in parameter hyperspace, may have a multim minima response surface because of the target data used making it difficult to obtain a global minimum in the search process. The existence of a stochastic or 'noisy' cost surface, which results in a proliferation of 'false' local minima about the global minimum, is unavoidable because of model complexity and depends on the accuracy with which inverter PWM switching instants with subsequent delay turnon are resolved during model simulation (Guinee et al, 1999). Furthermore the number of genuine local minima, besides cost function noise, is governed by the choice of data training record used as the target function in the objective function formulation which in the case of step response testing with motor current feedback is similar to a sinc function profile (Guinee et al, 2001). The cost function is, however, reduced to one of its local minima during identification, preferably in the vicinity of its global minimizer, with respect to the BLMD model parameter set to be extracted. The presence of local minima will result in a large spread of parameter estimates about the optimum value with model accuracy and subsequent controller performance very much dependent on the minimization technique adopted and initial search point chosen. Besides adequate system modelling there is thus a need for a good identification search strategy (Guinee et al, 2000). over a noisy multim minima response surface.

Adaptive control of dc servomotors rely on such techniques as Self Tuning pole assignment [Brickwedde, 1985; Weerasooriya et al, 1989; El-Sharkawi et al, 1990], Model Reference [Naitoh et al, 1987; Chalam, 1987] and Variable Structure Control (VSC) (El-Sharkawi et al, 1989) for preselected trajectory tracking performance in guidance systems and robustness in high performance applications. This is in response to changing process operating conditions (El-Sharkawi et al, 1994) typified by changing load inertia in robots, EVs and machine tools. The essential feature of adaptation is the regulator design (Astrom et al, *ibid*), in which the controller parameters are computed directly from the online input/output response of the system using implicit identification of the plant dynamics, based on the principle of general minimum variance control in the two former methods with slide mode control implementation in VSC. Although no apriori knowledge of the physical nature of the systems dynamics is required, identification in this scenario relies on the application of

black box linear system modelling of the motor and load dynamics. This modelling strategy is based on a general family of transfer function structures (Ljung, 1987; Johansson, 1993) with an ARMAX model being the most suitable choice (Dote, *ibid*; Ljung, *ibid*). The parameter estimates of the model predictor are then obtained recursively from pseudolinear regression at regular intervals of multiple sampling periods. This type of modelling approach is particularly suitable for conventional dc machine drives because of their near linear performance with constant field current despite the complex DSP solution of the adaptive controller. However the PM motor drive, in contrast, is essentially nonlinear both in terms of its operation electro-dynamically (Krause, 1986, 1989) and in the functionality of the switching converter where considerable dead time is required in the protective operation of the power transistor bridge network. When the state space method is employed in this case, as in for example variable structure tracking control, a considerable degree of idealization is introduced in the linearization of the model equations about the process operating point, which are essentially nonlinear, for controller design. The above modelling schemes therefore suffer from the drawback of not adequately describing nonlinearities encountered in real systems and are thus inaccurate. Furthermore in high performance PM drive applications, characterized by large excursion and rapid variation in the setpoint tracking signal, other nonlinearities such as magnetic saturation, slew rate limitation and dead zone effects are encountered in the dynamic range of operation. Effective modelling of the physical attributes of a real PM drive system (Guinee et al, 1998, 1999) is a therefore necessary prerequisite for controller design accuracy in high performance BLMD applications.

1.1 Objectives

This chapter is concerned with the presentation of a detailed model of a BLMD system including PWM inverter switching operation with dead time (Guinee, 2003). This model can then be used as an accurate benchmark reference to gauge the speed and torque performance characteristics of proposed embedded BLMD systems via simulation in EV applications. The decomposition of BLMD network structure into various subsystem component entities is demonstrated (Guinee et al, 1998). The physical modelling procedure of the individual subsystems into linear functional elements, using Laplacian transfer function synthesis, with non linearities described by difference equations is explained. The solution of the model equations using numerical integration techniques with very small step sizes (0.5% of PWM period T_s) is discussed and the application of the regula-falsi method for accurate resolution of natural sampled PWM edge transitions within a fixed time step is explained. Very accurate simulation traces are produced, based on step response transients, for the BLMD in torque control mode which has wide bandwidth configuration, when compared with similar test data for a typical BLMD system. BLMD model accuracy is further amplified by the high correlation of fit of unfiltered current feedback simulation waveforms with experimental test data, which exhibit the presence of high frequency carrier harmonics associated with PWM inverter switching. Model validation is provided with a goodness of fit measure based on motor current feedback (FC) using frequency and phase coherence. A novel delay compensation technique, with zener clamping of the triangular carrier waveform during PWM generation, is presented for simultaneous three-phase inverter dead time cancellation which is verified through BLMD waveform simulation (Guinee, 2005, 2009).

necessary, since these are uncoupled from the actual PWM process except for the dead time, for accurate BLMD simulation with minimal run time. This simplified low frequency model strategy, based on the fundamental component of the PWM process, can only be used when there is negligible inverter delay and is the approach that is adopted in such circumstances for simulation purposes as the ‘average’ BLMD model. The presence of inverter dead time, however, requires additional BLMD model processing in that the current flow direction must be checked in each phase, during every PWM switching period, in order to determine whether a delay pulse or correction term is to be added or subtracted to the fundamental signal components. Consequently the modulated pulse edge transitions have to be accurately known to include the exact instances of fixed delay triggering of the basedrives controlling power transistor inverter ON/OFF switching. Once a satisfactory BLMD model of sufficient functional accuracy has been generated and ‘mapped’ to an actual embedded drive system, through parameter identification of the motor dynamics, the addition of the outer velocity control loop can then be completed in a holistic BLMD model for ASD simulation. Correlation accuracy of this complete model with an actual ASD is established through subsequent step response simulation and comparison with experimental shaft velocity test data.

Power Supply Unit (Moog Series - T157)	
Power o/p = 18 kW	
3Φ rms Voltage i/p $U_s = 220$ V	
DC Voltage o/p $U_d = 310$ V _{DC}	
Motor Controller Unit (Moog Series - T158)	
Current o/p $I_C = 15$ A Continuous, 30 A Peak	
Motor Controller Optimizer [MCO-402B]	Lag Compensator: $K=19.5$, $\tau_a = 225\mu s$, $\tau_b = 1.5ms$
Max. Motor Speed $n_{max} = 10,000$ RPM	Inverter Transistor Blanking $\delta = 20\mu s$
Transistor Switching Frequency $f_s = 5$ kHz	Current Loop Bandwidth = 3 kHz
Brushless 1.5kW PM Servomotor (Moog Series - D314...L20)	
Continuous Stall Torque $M_O = 5.0$ Nm	Peak Torque $M_{max} = 15$ Nm
Continuous Stall Current $I_O = 9.3$ A	Nominal Speed ($U=310$ V) $n_n = 4000$ rpm
Mass without Brake $m = 5.1$ kg	Rotor Inertia $J = 2.8$ kg.cm ²
Mass Factor $M_O/m = 0.98$ Nm.kg ⁻¹	Dynamic Factor $M_O/J = 19,000$ s ⁻²
Volume Factor $M_O/V = 2.8$ Nm.m ⁻³	No. PM Rotor Pole Pairs $p = 6$
Torque Constant $K_T = 0.32$ Nm.A ⁻¹	Calculation Factor $1.5 K_T = 0.48$ Mm.A ⁻¹
Motor Terminal Resistance $R_{tt} = 1.5$ Ω	Motor Terminal Inductance $L_{tt} = 3.88$ mH
Mech. Time Constant $\tau_m = 1$ ms	Elec. Time Constant $\tau_e = 2.6$ ms

Table I. Moog BLMD System Component Specification

The motor drive system (Moog GmbH, *ibid*), used as the focus of investigation in the mathematical development of the BLMD system based on physical principles, is shown in Figure 1 and is typical of most high performance PM motor drives available. This drive system is required for verification and validation of the BLMD modelling process at critical internal observation nodes through comparison of experimental test results with model simulation runs for accuracy. The servomotor system consists of a Power Supply Unit, Motor Controller Unit and a PM brushless motor with component specification details as summarised in Table I. The BLMD system, that is modelled here, has a considerable inverter dead time (20μs) by comparison with the nominal PWM switching period (200μs). Each phase of the motor stator winding has a separate PWM current controller with a 20μs inverter delay for

protection from current ‘shoot through’. This delay, which is dependent on the direction of winding current flow, is manifested as a reduction in the overall modulated pulsewidth voltage supply to the stator winding and developed motor drive torque. If the current flow is directed into the phase winding then there is a reduction of $20\mu\text{s}$ at the leading edge of the modulated pulsewidth and if the current flow is negative an extension of $20\mu\text{s}$ is appended at the trailing edge of the modulated pulse. An accurate model of the BLMD system must account for the presence of such a delay. During simulation of the BLMD model the current flow direction has to be sensed to determine whether a fixed $20\mu\text{s}$ delay pulse is to be subtracted from or added to the modulated pulse duration. Detailed evaluation of the width modulated pulse edge transition times is required for accurate BLMD modelling in such circumstances in torque control mode to ensure numerical accuracy of PWM inverter simulation and subsequent positioning of the inverter trigger delay associated with the large dead time present. This is afforded by the use of small step sizes ($\sim 0.5\%T_s$) by comparison with the overall PWM switching period (T_s) and application of the regula-falsi iterative search method (Press et al, 1990) during BLMD simulation. Model accuracy is guaranteed through numerical waveform simulation, which is shown to give excellent agreement in terms of correlation with BLMD experimental test data at critical observation nodes for model fidelity purposes. Consequently the BLMD model can be used for the specific purpose of accurate simulation of circuit functionality within an actual typical EV motor drive system with special emphasis on the inner torque loop as it embraces the PWM motor current control operation with inverter delay during rapid EV acceleration.

2.1 Overall system description

The 1.5 kW motor drive system, used as the subject of this BLMD modelling procedure, has the component block diagram sketched in Figure 2. This system is an electronic self commutated, PM synchronous machine (Tomasek, 1979), which is sinusoidally controlled (Tomasek, 1986) and is typical of most high performance PM motor drives available. The BLMD consists of a Power Supply Unit (PSU), Motor Controller Unit (MCU) and a Brushless Servomotor with specification details itemized in Table I. The PSU converts the matched three phase (3Φ), $220V_{\text{rms}}$ mains supply (U_s) into a full wave rectified stiff 310 volt dc supply (U_d) with 18kW continuous power output thus permitting multiple motor controller connection. A large smoothing capacitor maintains a constant dc link voltage which provides a low impedance dc source for voltage-fed inverter operation. The PSU can also fitted with an external dynamic braking resistor which bleeds excess energy from the DC busbar U_d during motor regeneration when the ASD is overhauled by the rotor mechanical load. This resistor prevents overcharging of the filter capacitor and thus a rise in the DC link voltage during rapid deceleration. The MCU contains the following functional elements, as depicted in Figure 3, which are essential for proper operation of the brushless servomotor: (a) Power converter, (b) PWM modulator, (c) Current controller, (d) 3Φ commutator, (e) Velocity controller and (e) Circuit protection.

This provides brushless motor commutation and subharmonic PWM power control with a 30 Amp continuous output (o/p) current per phase to facilitate peak motor torque. The controller outputs a synthesized variable frequency and variable amplitude 3Φ sinusoidal current which accurately controls motor speed (n) and torque (Γ). This is facilitated by a configuration of six Darlingtion transistor-diode switches which form the three-leg inverter amplifier shown in Figure 1.

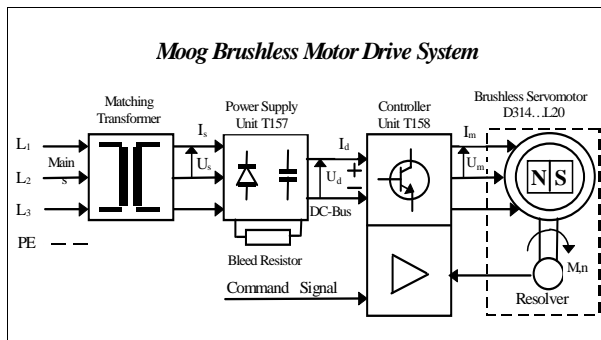


Fig. 2. Typical BLMD system components (Moog, 1989)

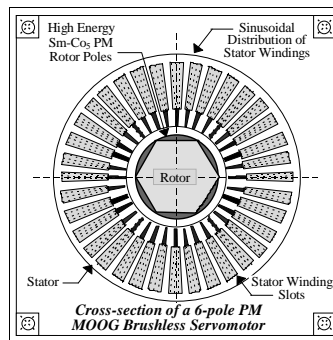


Fig. 4. Motor cross section

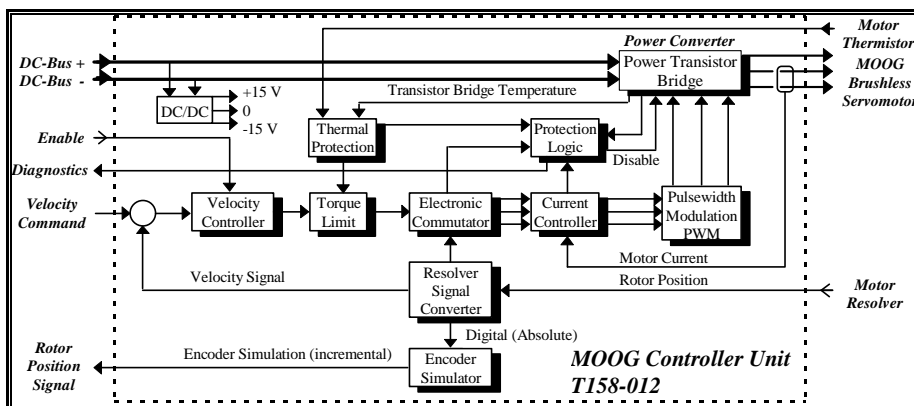


Fig. 3. Block schematic of a typical BLMD controller module

The brushless motor consists of a 12-pole PM rotor, a wound multiple pole stator, a 2-pole transmitter type pancake resolver and a ntc thermistor embedded in the stator end turns with a typical cross-section sketched in Figure 4. Stator current is provided by a 3Φ power cable with a protective earth while a signal cable routes rotor position information from the pancake resolver located at the rear side of the motor structure. The outer motor casing (stator) houses the 3Φ stationary winding in a lamination stack. The Y-connected floating neutral winding is embedded in slots around the air gap periphery with a sinusoidal spatial distribution. This has the effect of producing a time dependent rotating sinusoidal MMF space wave centred on the magnetic axes of the respective phases, which are displaced 120 electrical degrees apart in space. The inner member (rotor) contains the Samarium-Cobalt magnets, which have a high holding force with an energy product of 18 MGO_e (Demerdash et al, 1980), in the form of arc segments assembled as salient poles on an iron rotor structure. The fixed radially directed magnetic field, produced by the rotor magnets, is held perpendicular to the electromagnetic field generated by the stator coils and consequently yields maximum rotor torque for a given stator current. This stator-to-rotor vector field interaction is achieved by electronic commutation, which processes rotor position information from the shaft resolver to provide a balanced three phase sinusoidal stator current. The high peak torque achievable, which is

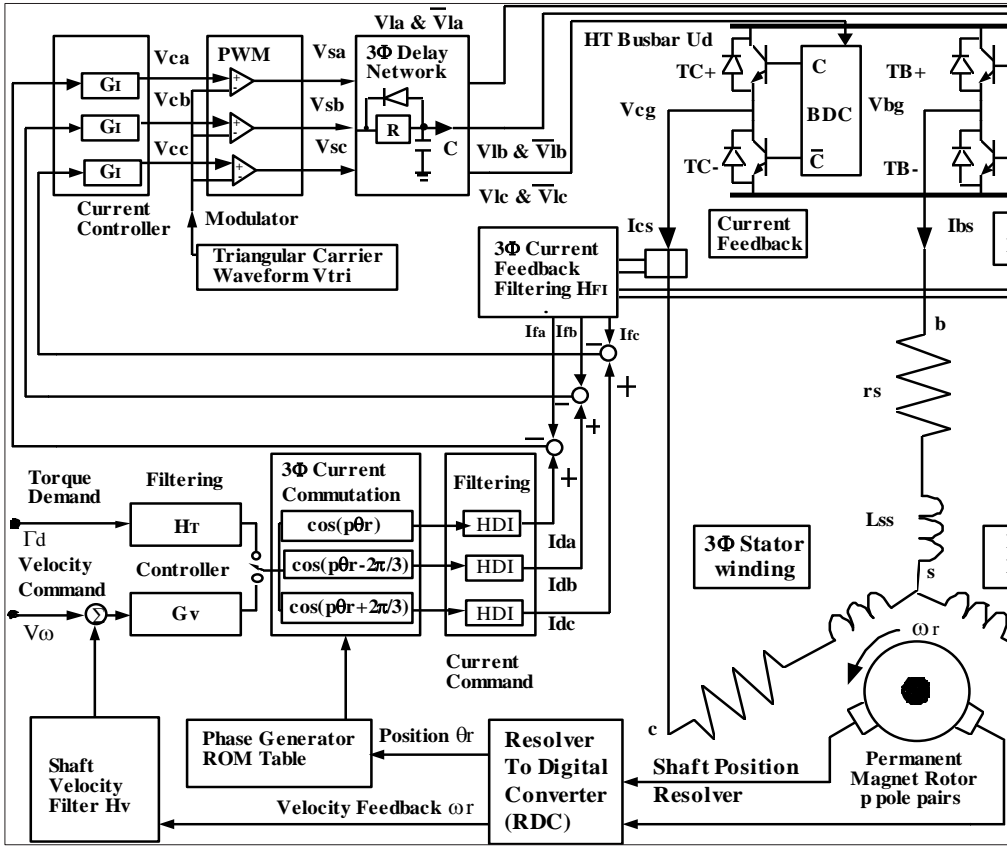
about eight to ten times the rated torque for Sm-Co₅ PM motors (Tomasek, 1983), and low rotor inertia J result in high dynamic motor performance which is evident from the large dynamic factor given in Table I. A high continuous torque-to-volume ratio is achieved due to the high pole number in the motor stator.

2.1.1 General features of a typical BLMD system

A network structure for this BLMD system, showing the functional subsystems and their interconnection into an overall organizational pattern, is illustrated in Figure 1A. This provides indication of the type and complexity of model required as the first step in the development of a comprehensive and accurate model for embedded system parameter identification and EV performance evaluation. The dynamic system consists of an inner current loop for torque control and an outer velocity loop for motor shaft speed control each of which can be individually selected according to the control operation required. The major functional elements of the system are:

- a. a velocity PI control governor G_V for wide bandwidth speed tracking. This compares the velocity command V_ω with the estimated motor shaft velocity $V\omega_r$ from the resolver-to-digital converter (RDC) and from which an optimized velocity error signal e_v is derived.
- b. a torque demand filter H_T with limiter for command input Γ_d slew rate limitation and circuit protection in the event of excessive temperature in the motor winding and MCU baseplate.
- c. a phase generation ROM lookup table which issues sinewaves corresponding to position of the rotor magnetic pole. The phase angles are determined, with angular displacement of 120 degrees apart, from the RDC position θ , for current vector $I(t)$ commutation
- d. a 3Φ commutation circuit for generation of variable frequency and variable amplitude phase sequence current command signals. The command amplitudes are determined by mixing the velocity error or torque demand with the phase generator output using an 8-bit multiplying Digital-to-Analog Converter (DAC).
- e. current command low pass filtering H_{DI} for high frequency harmonic rejection.
- f. current controllers G_I which close a wide bandwidth current loop around three phases of the motor winding in response to the filtered commutator current output. Current feedback sensing from the stator windings is accomplished through Hall Effect Devices (HED) which is then filtered (H_{FI}) to remove unwanted noise.
- g. a 3Φ pulse width modulator giving an output set of amplitude limited ($\pm V_S$) switching pulse trains to drive the inverter power transistor bridge. The pulse aperture times are modulated by the error voltages from the respective phase current controllers when compared with a fixed frequency triangular waveform $v_{tri}(t)$.
- h. RC delay networks which provide a fixed delay δ , related to the turn-off time of power transistors, between inverter switching instants. These "lockout" circuits are necessary during commutation of the inverter power transistors to avoid dc link short circuit with current "shoot-through".
- i. a six step inverter which consists of the PWM controlled three-leg power transistor bridge and the base drive circuitry which include the switch delay networks. As the motor rotates the commutation logic switches over the power transistor bridge legs via the base drive circuits in a proper sequence. During a given commutation interval the power transistor bridge is reduced to one of the three possible (a-b, a-c, b-c) two-leg configurations. The PWM pulse trains are effectively amplified to the dc bus voltage supply U_d before application to the three phase motor stator windings.

Fig. 1A. Network structure of a typical brushless motor drive system (Guinee, 1998)



- j. an RDC (Figure 1A) which provides a 12 bits/rev natural binary motor shaft position signal, with the 10MSB's used for motor commutation, and an analogue linear voltage signal proportional to motor speed ω_r . The estimated speed signal is subsequently filtered to give a velocity tracking signal $V\omega_r$ which can be used for motor tuning via G_V and performance evaluation.
- k. a shaft velocity filter H_V for speed signal noise reduction before feeding to the velocity controller.
- l. three phase motor with a high coercivity permanent magnet rotor.

2.2 Mathematical behavioural model of BLMD system

The behaviour of the BLMD system can be ascertained from physical principles in terms of its electromechanical operation during energy conversion. The system operation is described in terms of its Kirchhoff's law voltage equations and electromagnetic torque which are derived in subsequent sections. These equations can be used to

- a. develop a complete mathematical model for the BLMD system whereby its performance can be evaluated
- b. understand and analyse the electromechanical energy conversion process in the PM motor and
- c. in system design techniques and optimization for specific requirements.

The result is a set of nonlinear equations describing the dynamic performance of the BLMD system. The 3 Φ motor stator windings are \mathbf{Y} connected and are sinusoidally distributed with an angular separation of $2\pi/3$ radians, associated with the mechanical location of the phase coils, as illustrated in Figure 4. The rotor consists of p pairs of permanent magnet pole face slabs, anchored to the solid steel shaft, which provide a sinusoidal magnetic flux distribution vector $\mathbf{\Lambda}(\theta_r)$ in the air gap between the rotor and stator. If the PM pole face geometry admits to a nonuniform air gap then the reluctance variation, due to the effects of rotor saliency, as a function of rotor position is generally considered in the evaluation of the stator winding inductances. The effects of rotor saliency as shown in Figure 5, where the a_s , b_s , c_s and d axes denote the positive direction of the magnetic axes of the symmetrical windings and PM poles in stationary (s) and rotating (r) coordinate reference frames, will be included initially as a generalization of the analytical model of the BLMD system.

2.2.1 Stator winding flux linkages and inductances

Angular displacements can be referred to either the rotor or stator frames as shown in Figure 5 with the interrelationship

$$\phi_s = \phi_r + \theta_r \quad (I)$$

where ϕ_s and θ_r are the respective stator and rotor angular displacements referred to the \mathbf{a}_s axis. The air-gap MMF space vector for the 3 Φ distributed stator winding, with N_s equivalent coil turns per phase, can be written in terms of the space angle $p\phi_s$ around the air gap periphery as

$$\mathfrak{F}_s(\phi_s, t) = \begin{bmatrix} \mathfrak{F}_{as} \\ \mathfrak{F}_{bs} \\ \mathfrak{F}_{cs} \end{bmatrix} = \left(\frac{N_s}{2p}\right) \begin{bmatrix} i_{as} \cos(p\phi_s) \\ i_{bs} \cos(p\phi_s - \frac{2\pi}{3}) \\ i_{cs} \cos(p\phi_s + \frac{2\pi}{3}) \end{bmatrix} \quad (II)$$

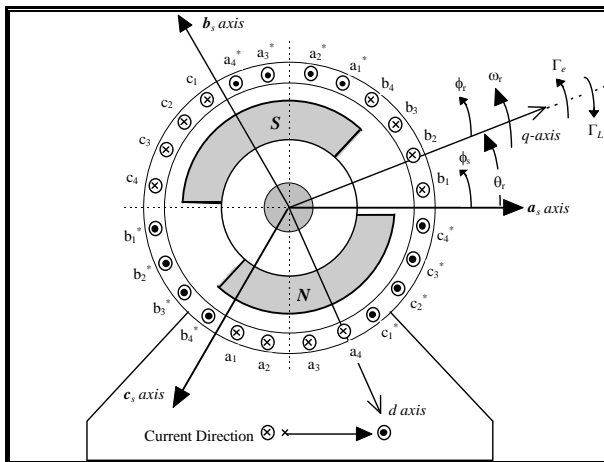


Fig. 5. Salient 2-pole synchronous PM Motor with non-uniform air gap (Guinee, 2003)

The MMF standing wave, which is wrapped around the air gap periphery, is effectively produced by a sinusoidally distributed current sheet located on the inner stator circumference as shown in Figure 6 for phase-a. The standing space wave components are modulated by the time varying balanced 3Φ stator current, with electrical angular frequency ω_e , represented by

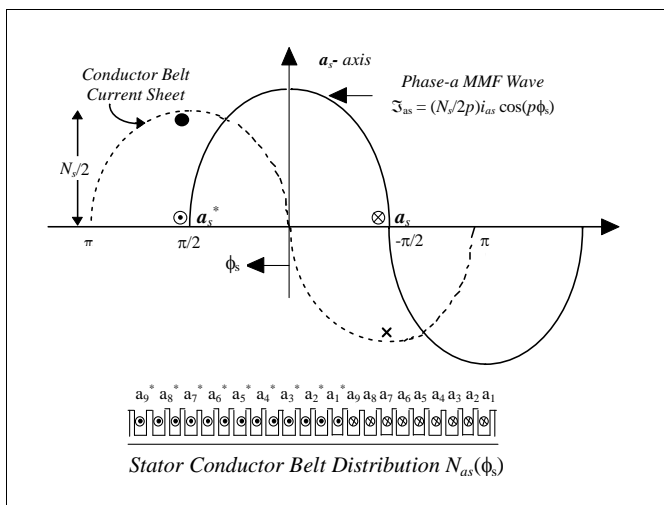


Fig. 6. Phase-a MMF standing space wave

$$\mathbf{I}_s(t) = \begin{bmatrix} i_{as}(t) \\ i_{bs}(t) \\ i_{cs}(t) \end{bmatrix} = \begin{bmatrix} I_m \cos(\omega_e t) \\ I_m \cos(\omega_e t - \frac{2\pi}{3}) \\ I_m \cos(\omega_e t + \frac{2\pi}{3}) \end{bmatrix} \tag{III}$$

These pulsating standing waves, with amplitudes proportional to the instantaneous phase currents and directed along the magnetic axes of the respective phases, produce a travelling MMF_s wave that rotates counterclockwise about the air gap as a set of magnetic poles given by

$$\mathfrak{F}_s(\phi_s, t) = \left(\frac{3}{2}\right) \left(\frac{N_s}{p} I_m\right) \cos(\omega_e t - p\phi_s) \tag{IV}$$

with synchronous speed

$$\frac{d\phi_s}{dt} = \frac{\omega_e}{p} = \omega_r \tag{V}$$

The motor shaft also rotates at synchronous speed with the result that the stator MMF is stationary with respect to the rotor. The length of the air gap $g(\phi)$ between the rotor and stator changes with rotor position ϕ , which for a $2p$ -pole rotor, using Figure 5, is given by $g(\phi) = (\alpha_1 - \alpha_2 \cos(2p\phi_r))^{-1}$ with upper and lower bound limits given as $(\alpha_1 + \alpha_2)^{-1} \leq g \leq (\alpha_1 - \alpha_2)^{-1}$. Consequently this affects the reluctance of the flux path with a cyclic variation that occurs $2p$ times during one period of revolution of the rotor. As a result of reluctance variation, the inductances of the stator windings change periodically with PM pole rotation. The net magnetic flux in the motor air gap can be regarded as a combination of that due to the rotating armature MMF and a separate independent PM polar field contribution. The effect of armature reaction MMF on the magnitude and distribution of the air gap flux in a PM motor can be controlled by altering the winding current using an electronic converter which is self-synchronized by a shaft position sensor as in a BLMD system. The corresponding flux density radial vector $B_s(\phi_s, \theta_r)$ contributions in the air gap can be determined from the MMF for each phase acting separately due to its own current flow, using Ampere’s magnetic circuit law, as

$$\mathbf{B}_s(\phi_s, \theta_r) = \begin{bmatrix} B_{as} \\ B_{bs} \\ B_{cs} \end{bmatrix} = \frac{\mu_0}{g(p\phi_s - p\theta_r)} \begin{bmatrix} \mathfrak{F}_{as} \\ \mathfrak{F}_{ab} \\ \mathfrak{F}_{cs} \end{bmatrix} \tag{VI}$$

The flux linkage $\Phi_s(\phi_s, \theta_s)$ of a single turn of a stator winding, which spans π radians with angular orientation ϕ_s from the a_s axis, can be determined by integration (Krause, *ibid*) as

$$\Phi_s(\phi_s, \theta_r) = \int_{\phi_s}^{\phi_s + \pi/p} B_s(\xi, \theta_r) r l d\xi \tag{VII}$$

over the cylindrical surface defined by the air gap mean radius r and axial length l . The flux linkage of an entire stator phase winding, due to its own current flow, can be determined from integration over all turns of a conductor belt with sinusoidal distribution $N_s(\phi_s)$ given by

$$\mathbf{N}_s(\phi_s) = \begin{bmatrix} N_{as} \\ N_{bs} \\ N_{cs} \end{bmatrix} = \left(\frac{N_s}{2p}\right) \begin{bmatrix} \sin(p\phi_s) \\ \sin(p\phi_s - \frac{2\pi}{3}) \\ \sin(p\phi_s + \frac{2\pi}{3}) \end{bmatrix} \tag{VIII}$$

If linear magnetic structures are assumed for non saturated stator conditions the flux linkage for phase-a, with similar calculations for the other two phases, is given by

$$\begin{aligned} \lambda_{asas} &= L_{ls}i_{as} + p \int_0^{\pi/p} N_{as}(\phi_s)\Phi_{as}(\phi_s, \theta_r)d\phi_s \\ &= L_{ls}i_{as} + \left(\frac{N_s}{2p}\right)^2 p\pi\mu_0rl\left(\alpha_1 - \frac{\alpha_2}{2}\cos(2p\theta_r)\right)i_{as} \end{aligned} \tag{IX}$$

where L_{ls} is the leakage inductance. The second term in (IX), when divided by the current i_{as} , defines the phase-a winding self inductance

$$L_{asas} = L_{ss} - L_G \cos(2p\theta_r) \tag{X}$$

with $L_{ss} = \left(\frac{N_s}{2p}\right)^2 p\pi\mu_0rl\alpha_1$ and $L_G = \frac{1}{2}\left(\frac{N_s}{2p}\right)^2 p\pi\mu_0rl\alpha_2$. This consists of the nominal inductance L_{ss} as the default value for round rotor geometry and the variable air gap reluctance contribution which pulsates with amplitude L_G with rotor position. Similar self inductance expressions can be deduced for the other two phases, by allowing for the 120° phase displacement in the air gap reluctance contribution, as

$$\begin{aligned} L_{bsbs} &= L_{ss} - L_G \cos 2(p\theta_r - \frac{2\pi}{3}) \\ L_{cscs} &= L_{ss} - L_G \cos 2(p\theta_r + \frac{2\pi}{3}) \end{aligned} \tag{XI}$$

The flux linkage contribution from mutual magnetic coupling between phases is obtained, via (IX), by evaluating the flux linking of a particular phase winding due to current flow in any of the two other phases. The magnetic interaction between phases a and b, for example, is given by

$$\begin{aligned} \lambda_{asbs} &= \int N_{as}(\phi_s)\Phi_{bs}(\phi_s, \theta_r)d\phi_s = -\left(\frac{N_s}{2p}\right)^2 p\frac{\pi}{2}\mu_0rl\left[\alpha_1 + \alpha_2 \cos(2p\theta_r - \frac{2\pi}{3})\right]i_{bs} \\ &= \left[-\frac{1}{2}L_{ss} - L_G \cos(2p\theta_r - \frac{2\pi}{3})\right]i_{bs} \end{aligned} \tag{XII}$$

with similar expressions for the other cross phase interactions. The corresponding mutual inductance is determined as, upon dividing (XII) by i_{bs} ,

$$L_{asbs} = L_{bsas} = -\frac{1}{2}L_{ss} - L_G \cos(2p\theta_r - \frac{2\pi}{3}) \tag{XIII}$$

This consists of the nominal value ($-L_{ss}/2$) normally associated with a uniform air gap or round rotor and a variable component due to rotor saliency. The mutual inductance components associated with other flux linkage phase interactions are reciprocal and are similarly obtained with

$$\begin{aligned} L_{ascs} &= L_{csas} = -\frac{1}{2}L_{ss} - L_G \cos(2p\theta_r + \frac{2\pi}{3}) \\ L_{bscs} &= L_{csbs} = -\frac{1}{2}L_{ss} - L_G \cos(2p\theta_r) \end{aligned} \tag{XIV}$$

The cumulative flux linkage for each of the three phases, using (IX) and (XII) as examples for phase-a, may be expressed as

$$\Lambda_s(\mathbf{I}, \theta_r) = [\lambda_{as} \quad \lambda_{bs} \quad \lambda_{cs}]^T \tag{XV}$$

with

$$\begin{aligned} \lambda_{as} &= \lambda_{asas} + \lambda_{asbs} + \lambda_{ascs} + \lambda_{asm} = \lambda_{ass} + \lambda_{asm} \\ \lambda_{bs} &= \lambda_{bsas} + \lambda_{bsbs} + \lambda_{bscs} + \lambda_{bsm} = \lambda_{bss} + \lambda_{bsm} \\ \lambda_{cs} &= \lambda_{csas} + \lambda_{csbs} + \lambda_{cscs} + \lambda_{csm} = \lambda_{css} + \lambda_{csm} \end{aligned}$$

where $\{\lambda_{asm}, \lambda_{bsm}, \lambda_{csm}\}$ represent the PM rotor phase-flux linkages which have a 120° relative phase disposition and $\{\lambda_{ass}, \lambda_{bss}, \lambda_{css}\}$ are the 3-phase armature reaction flux linkages. The general form of the flux linkage expression (XV) can be evaluated, via (IX) and (XII), using numerical integration techniques without resorting to the linear magnetic circuit constraint. This approach is relevant only when magnetic saturation is an issue during very high current demand in peak torque applications. In this instance the time varying inductances, associated with salient PM rotor rotation, are nonlinear with values that depend on the saturation status of the armature iron. However the assumption of linear magnetic structures greatly simplifies the modelling process with considerable savings in numerical computation. This assumption is applicable in the absence of magnetic saturation and can be used to provide a very good model approximation with negligible error during brief periods of magnetic saturation associated with over current drive. The total magnetic flux vector $\Lambda_s(I, \theta_r)$ may be rewritten in terms of winding inductance matrix $L_s(\theta_r)$, stator current $I_s(t)$ and rotor field coupling $\Lambda_{sm}(\theta_r)$, for linear magnetic operation, as

$$\begin{bmatrix} \lambda_{as} \\ \lambda_{bs} \\ \lambda_{cs} \end{bmatrix} = \begin{bmatrix} L_{ls} + L_{asas} & L_{asbs} & L_{ascs} \\ L_{bsas} & L_{ls} + L_{bsbs} & L_{bscs} \\ L_{csas} & L_{csbs} & L_{ls} + L_{cscs} \end{bmatrix} \begin{bmatrix} i_{as} \\ i_{bs} \\ i_{cs} \end{bmatrix} + \begin{bmatrix} \lambda_{asm} \\ \lambda_{bsm} \\ \lambda_{csm} \end{bmatrix} \tag{XVI}$$

This can also be expressed in the compact matrix form as

$$\Lambda_s(\mathbf{I}, \theta_r) = \Lambda_{ss}(\mathbf{I}, \theta_r) + \Lambda_{sm}(\theta_r) = \mathbf{L}_s(\theta_r)\mathbf{I}_s(t) + \Lambda_{sm}(\theta_r) \tag{XVII}$$

with total flux $\Lambda_s(\mathbf{I}, \theta_r) = [\lambda_{as} \quad \lambda_{bs} \quad \lambda_{cs}]$, rotor flux

$$\Lambda_{sm}(\theta_r) = [\lambda_{asm} \quad \lambda_{bsm} \quad \lambda_{csm}]^T = \left[\lambda_m \sin(p\theta_r) \quad \lambda_m \sin\left(p\theta_r - \frac{2\pi}{3}\right) \quad \lambda_m \sin\left(p\theta_r + \frac{2\pi}{3}\right) \right]^T$$
 and stator

$$\text{flux } \Lambda_{ss}(\mathbf{I}, \theta_r) = [\lambda_{ass} \quad \lambda_{bss} \quad \lambda_{css}]^T = \mathbf{L}_s(\theta_r)\mathbf{I}_s(t)$$

Since the machine windings are Y-connected the algebraic sum of the branch currents is zero with

$$i_{as} + i_{bs} + i_{cs} = 0 \tag{XVIII}$$

and the flux linkage equation (XVI) can be written in terms of the symmetric inductance matrix as

$$\begin{bmatrix} \lambda_{as} \\ \lambda_{bs} \\ \lambda_{cs} \end{bmatrix} = \begin{bmatrix} L_{ls} + L_s - L_G \cos(2p\theta_r) & -L_G \cos(2p\theta_r - \frac{2\pi}{3}) & -L_G \cos(2p\theta_r + \frac{2\pi}{3}) \\ -L_G \cos(2p\theta_r - \frac{2\pi}{3}) & L_{ls} + L_s - L_G \cos(2p\theta_r + \frac{2\pi}{3}) & -L_G \cos(2p\theta_r) \\ -L_G \cos(2p\theta_r + \frac{2\pi}{3}) & -L_G \cos(2p\theta_r) & L_{ls} + L_s - L_G \cos(2p\theta_r - \frac{2\pi}{3}) \end{bmatrix} \begin{bmatrix} i_{as} \\ i_{bs} \\ i_{cs} \end{bmatrix} + \begin{bmatrix} \lambda_{asm} \\ \lambda_{bsm} \\ \lambda_{csm} \end{bmatrix} \tag{XIX}$$

where L_s is the synchronous inductance for a non salient rotor given by $L_s = \frac{3}{2}L_{ss}$. If leakage inductance is neglected and a round rotor structure is assumed the inductance variation L_G in (XIX) disappears with the elimination of the air gap factor α_2 . This results in the synchronous inductance matrix, which is diagonal, with constant entries L_s .

The phase voltage equations governing the BLMD electrical behaviour can be determined from the stator winding flux linkages using Faraday's law as follows

$$\mathbf{V}_s(t) = \mathbf{R}_s \mathbf{I}_s(t) + \frac{d\Lambda_s(l,t)}{dt} = \mathbf{R}_s \mathbf{I}_s(t) + \mathbf{L}_s(\theta_r) \frac{d\mathbf{I}_s(t)}{dt} + \mathbf{I}_s(t) \frac{d\mathbf{L}_s(\theta_r)}{dt} + \frac{d\Lambda_{sm}(\theta_r)}{dt} \tag{XX}$$

which phase index notation change $\{1 \equiv a; 2 \equiv b; 3 \equiv c\}$ where $\mathbf{V}_s(t) = [v_{1s}(t) \ v_{2s}(t) \ v_{3s}(t)]^T$, $\mathbf{I}_s(t) = [i_{1s}(t) \ i_{2s}(t) \ i_{3s}(t)]^T$, $\mathbf{R}_s = \text{diag}[r_s]$ and r_s is the phase winding resistance and $L_s(\theta_r)$ is the time varying inductance matrix in (XIX).

2.2.2 Phase voltage equations in the stator reference frame

The voltage expression (XX) in stationary coordinates is used to determine the phase voltage differential equations based on the assumption of a round rotor structure as follows:

$$v_{js} = r_s i_{js} + \frac{d\lambda_{js}(i_{js}, \theta_r)}{dt} \text{ for } j = 1, 2, 3 \tag{XXI}$$

The total mutual air gap magnetic flux for phase- j given by

$$\lambda_{js}(i_{js}, \theta_r) = \lambda_{jss}(i_{js}, \theta_r) + \lambda_{mij}(\theta_r) = L_s i_{js} + \lambda_{mij}(\theta_r) \tag{XXII}$$

where

$$\lambda_{mij}(\theta_r) = \lambda_m \sin(p\theta_r - \frac{2(j-1)\pi}{3}).$$

Expression (XXI) may be rewritten as

$$v_{js} = r_s i_{js} + L_s di_{js}/dt + v_{ej} \text{ for } j = 1, 2, 3 \tag{XXIII}$$

where v_{ej} is the internally generated phase- j back emf voltage given by

$$v_{ej} = K_e \omega_r \cos(p\theta_r - \frac{2(j-1)\pi}{3}) \tag{XXIV}$$

with motor voltage back EMF constant K_e given by $K_e = p\lambda_m$ and rotor shaft velocity ω_r as in (V). The alternative compact matrix form for (XXIII) is given by

$$\begin{bmatrix} v_{1s} \\ v_{2s} \\ v_{3s} \end{bmatrix} = \begin{bmatrix} r_s & 0 & 0 \\ 0 & r_s & 0 \\ 0 & 0 & r_s \end{bmatrix} \begin{bmatrix} i_{1s} \\ i_{2s} \\ i_{3s} \end{bmatrix} + \begin{bmatrix} L_{ls} + L_s & 0 & 0 \\ 0 & L_{ls} + L_s & 0 \\ 0 & 0 & L_{ls} + L_s \end{bmatrix} \cdot \frac{d}{dt} \begin{bmatrix} i_{1s} \\ i_{2s} \\ i_{3s} \end{bmatrix} + K_e \begin{bmatrix} \cos(p\theta_r) \\ \cos(p\theta_r - \frac{2\pi}{3}) \\ \cos(p\theta_r + \frac{2\pi}{3}) \end{bmatrix} \tag{XXV}$$

The uniform air gap assumption results in a diagonal inductance matrix, which allows for current variable decoupling in (XXV) and thus a tractable model structure. This approach is somewhat justified, in the absence of magnetic saturation, from previous studies (Persson et al, 1976; Demerdash et al, 1980) where the independence of stator inductance with salient

rotor displacement has been explained. The *raison d'être* of this simplifying assumption is that the permeability of the magnetically hard Samarium-Cobalt (SmCo_5) material is almost equal to that of air. As a consequence of this property the SmCo_5 material has some desirable features from a BLMD modelling perspective in terms of its intrinsic demagnetization characteristic. The PM rotor air gap line (Matsch, 1972) is a design feature which is optimized in terms of the maximum energy product of 160 kJm^{-3} (Crangle, 1991) for a given machine configuration and magnet geometry. In Figure 7 the locus of operation of the air gap line, due to changes in gap width, is a minor hysteresis loop (Match, *ibid*) with axis tangent to the magnetization curve through the retention flux Φ_0 .

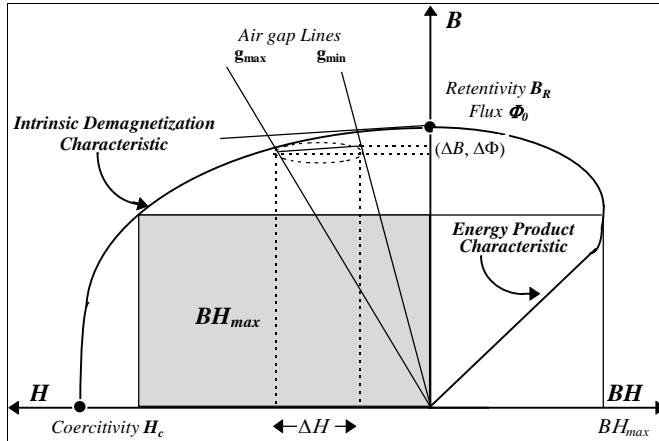


Fig. 7. PM flux variation with air gap width

The corresponding oscillating PM flux variations $\Delta\Phi$, which occur p times per rotor revolution, are practically negligible ($\Delta\Phi \ll \Phi_0$) with little impact on the overall rotor flux linkage contribution to the stator windings.

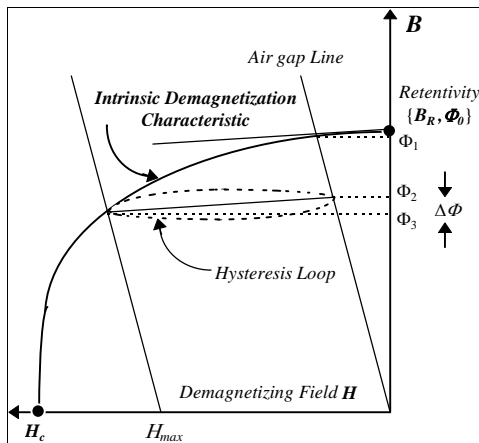


Fig. 8. Demagnetizing MMF effect

In Figure 8 the repeated application of a demagnetizing MMF, generated by the stator windings, results in a negligibly small flux variation ($\Delta\Phi \ll \Phi_0$) associated with the minor hysteresis loop on the demagnetization curve. The applied radial stator H -field, which is designed to lie on the knee of the intrinsic demagnetization characteristic (Pesson et al, 1976) corresponding to the energy product figure BH_{max} , has its maximum value associated with the air gap line at H_{max} . Since the PM relative permeability (μ_r) is almost unity, the applied field generated in the stator windings is not affected by rotor position.

2.2.3 Electromechanical energy conversion and torque production

In a BLMD system the electromechanical energy conversion process involves the exchange of energy between the electrical and mechanical subsystems through the interacting medium of a magnetic coupling field. This energy transfer mechanism is manifested by the action of the coupling field on output mechanical motion of the rotor shaft masses and its stator winding input reaction to the electrical power supply. This reaction, which is necessary for the coupling field to absorb energy from the electrical supply, is the emf $V_s^*(t)$ induced across the coupling field by the magnetic field interaction of the stator winding with the PM rotor. Energy conversion during motor action is maintained by the incremental supply of internal electrical energy dW_e , associated with sustained current flow $I_s(t)$ against the reaction emf, to balance the differential energy dW_f absorbed by the reservoir coupling field and that released by the coupling field dW_m to mechanical form. This results in the replenished energy transfer for sustained motion with stator flux change $d\Lambda_s(I, \theta_r)$, using (V), as

$$dW_e = I_s(t)V_s^*(t)dt = I_s(t)d\Lambda_s(I, \theta_r) = dW_f + dW_m \tag{XXVI}$$

where mechanical and field losses are included in the electrical source $V_s^*(t)$ and are thus ignored for convenience. In a motor system most of the stator winding MMF is used to overcome the reluctance of the air gap separating the fixed armature from the moving rotor in the magnetic circuit. Consequently most of the magnetic field energy is stored in the air gap so that when the field is reduced most of this energy is returned to the electrical source. Furthermore since stacked ferromagnetic laminations are used in the stator winding assembly the magnetic field core losses are minimal whereupon the magnetic coupling fields are assumed conservative. The field energy state function $W_f(\lambda_{1s}, \lambda_{2s}, \lambda_{3s}, \theta_r)$ can be expressed in terms of the flux linkages ($\lambda_{1s}, \lambda_{2s}, \lambda_{3s}$) in (XVI), for multiple stator winding controlled excitations with appropriate index change, and the mechanical angular displacement θ_r of the rotor. This can be expressed in differential form using (XXVI) in terms of the stator winding flux linkages λ_{js} and currents i_{js} as

$$dW_f = \sum_{j=1}^3 \frac{\partial W_f}{\partial \lambda_{js}} d\lambda_{js} + \frac{\partial W_f}{\partial \theta_r} d\theta_r = \sum_{j=1}^3 i_{js} d\lambda_{js} - dW_m \tag{XXVII}$$

The mechanical energy transfer dW_m with incremental change $d\theta_r$ in rotor position θ_r due to developed electromagnetic torque $\Gamma_e(I_s, \theta_r)$ by the coupling field is expressed by

$$dW_m = \Gamma_e(I_s, \theta_r) d\theta_r \tag{XXVIII}$$

By coefficient matching the state variables θ_r and λ_{js} for $j \in \{1, 2, 3\}$ in (XXVII) and (XXVIII) an analytical expression for the electromagnetic (EM) torque Γ_e is obtained with

$$\Gamma_e(\Lambda_s, \theta_r) = - \frac{\partial W_f(\Lambda_s, \theta_r)}{\partial \theta_r} \tag{XXIX}$$

in terms of the coupling field stored energy as a function of the flux linkages Λ_s . The coupling field energy is first determined by integration of the other coefficient partial differential equations

$$i_{js} = \frac{\partial W_f(\Lambda_s, \theta_r)}{\partial \lambda_{js}} \quad \forall j \in \{1,2,3\} \tag{XXX}$$

with respect to the flux linkages of the connected system for restrained rotor conditions as

$$W_f(\Lambda_s, \theta_r) \Big|_{(d\theta_r=0)} = \sum_j \int \frac{\partial W_f(\Lambda_s, \theta_r)}{\partial \lambda_{js}} d\lambda_{js} = \sum_{j=1}^3 \int i_{js} d\lambda_{js}(i_{1s}, i_{2s}, i_{3s}, \theta_r) \tag{XXXI}$$

as shown in Figure 9 before evaluation of the drive torque. Since the flux linkages are functions of the stator winding current, complex and lengthy numerical integration of (XXX) would be required over the nonlinear λ - i magnetization characteristic in Figure 9, which must be known, if saturation effects are to be included. However if magnetic nonlinearity is neglected, with the assumption that the flux linkages and MMFs are directly proportional for the entire magnetic circuit as in air, the resulting analysis and integral expression (XXXI) is greatly simplified. In this case the flux linkages are assumed to be linear with current magnitude, which is often done in the analysis of practical devices, in the winding inductances as in (XXII). However a simpler and more convenient alternative (Krause, 1986) than obtaining the EM torque as a function of Λ_s via $W_f(\Lambda_s, \theta_r)$ in (XXXI), relies on the coenergy state function $W_c(I_s, \theta_r)$ to determine the applied torque Γ_e in terms of the stator currents I_s as the independent PWM controlled state variables in BLMD system operation. This methodology is more effective during BLMD model simulation as the motor winding currents are immediately available for motor torque computation.

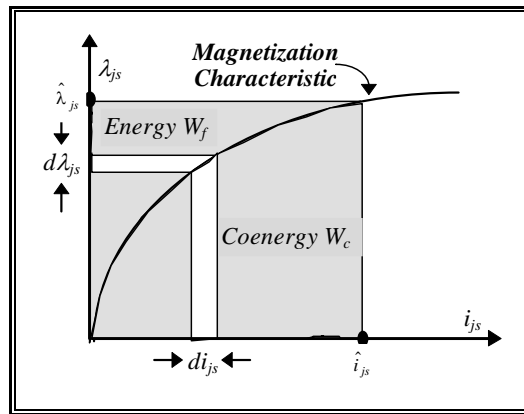


Fig. 9. Stored energy and coenergy

The coenergy $W_c(I_s, \theta_r)$, which has no physical basis or use other than to simplify the torque calculation, is the dual form of the coupling field energy $W_f(\Lambda_s, \theta_r)$ as shown in Figure 9 with

$$W_c(I_s, \theta_r) = \hat{I}_s^T \hat{\Lambda}_s - W_f(\Lambda_s, \theta_r) \tag{XXXII}$$

The following equivalent expressions result for the differential forms of the coenergy in (XXXII) using the substitutions (XVII) and (XVIII) for $W_c(\mathbf{I}_s, \theta_r)$

$$dW_c(\mathbf{I}_s, \theta_r) = \left[\sum_{j=1}^3 (i_{js} d\lambda_{js} + \lambda_{js} di_{js}) \right] - \left[\sum_{j=1}^3 i_{js} d\lambda_{js} - \Gamma_e(\mathbf{I}_s, \theta_r) d\theta_r \right] \tag{XXXIII}$$

$$dW_c(\mathbf{I}_s, \theta_r) = \sum_{j=1}^3 \frac{\partial W_c}{\partial i_{js}} di_{js} + \frac{\partial W_c}{\partial \theta_r} d\theta_r \tag{XXXIV}$$

which when coefficient matched yield the parametric equations

$$\lambda_{js} = \frac{\partial W_c(\mathbf{I}_s, \theta_r)}{\partial i_{js}} \quad \forall j \in \{1, 2, 3\} \tag{XXXV}$$

$$\Gamma_e(\mathbf{I}_s, \theta_r) = \frac{\partial W_c(\mathbf{I}_s, \theta_r)}{\partial \theta_r} \tag{XXXVI}$$

The coupling field coenergy is determined from (XXXV) by integrating the cumulative stator flux linkages in (XV) with respect to the appropriate phase currents for restrained rotor movement as

$$W_c(\mathbf{I}_s, \theta_r) = \int \sum_{j=1}^3 \frac{\partial W_c(\mathbf{I}_s, \theta_r)}{\partial i_{js}} di_{js} = \int \sum_{j=1}^3 \lambda_{js} di_{js} \tag{XXXVII}$$

If magnetic nonlinear saturation effects and field losses are negligible then the flux linkages are linearly related to the currents, which establish the magnetic coupling field, through the inductance circuit elements as in (XIX) for a salient pole rotor with

$$\lambda_{js} = \sum_{k=1}^3 (L_{jk} i_{ks} + \lambda_{jm}) \tag{XXXVIII}$$

The resulting coenergy W_c from substitution of (XXXVIII) into (XXXVII), is given by

$$W_c(\mathbf{I}_s, \theta_r) \Big|_{d\theta_r=0} = \frac{1}{2} \sum_{j=1}^3 L_{jj} \cdot i_{js}^2 + \sum_{j=1}^3 \sum_{\substack{k=1 \\ k \neq j}}^3 L_{jk} i_{ks} i_{js} + \sum_{j=1}^3 \lambda_{jm} \cdot i_{js} \tag{XXXIX}$$

from which the EM torque is evaluated using (XXXVI) as

$$\Gamma_e(\mathbf{I}_s, \theta_r) = \frac{1}{2} \sum_{j=1}^3 i_{js}^2 \frac{dL_{jj}}{d\theta_r} + \sum_{j=1}^3 \sum_{\substack{k=1 \\ k \neq j}}^3 i_{ks} i_{js} \frac{dL_{jk}}{d\theta_r} + \sum_{j=1}^3 i_{js} \frac{d\lambda_{jm}}{d\theta_r} \tag{XL}$$

This may be expanded in terms of the stator winding inductances for a salient pole machine as

$$\Gamma_e(\mathbf{I}_s, \theta_r) = pL_G \sum_{j=1}^3 \left[\sin\left(2p\theta_r - \frac{2(j-1)\pi}{3}\right) \cdot i_{js}^2 + 2 \sum_{\substack{k=1 \\ k \neq j}}^3 \sin\left(2p\theta_r - \frac{2(k-1)\pi}{3}\right) \cdot i_{ks} i_{js} \right] + K_t \sum_{j=1}^3 \cos\left(p\theta_r - \frac{2(j-1)\pi}{3}\right) i_{js} \tag{XLI}$$

with torque constant $K_t = p\lambda_m$ which is the same as K_e if proper units are used. If a round rotor structure is assumed, then the L_G terms in (XLI) disappear and the resulting developed motor torque, due to the coupling field reaction EMF, in general terms is given by

$$\begin{aligned} \Gamma_e(\mathbf{I}_s, \theta_r) &= \sum_{j=1}^3 i_{js} \frac{d\lambda_{jm}}{d\theta_r} = \sum_{j=1}^3 p\lambda_m \cos\left(p\theta_r - \frac{2(j-1)\pi}{3}\right) \cdot i_{js} \\ &= K_e \sum_{j=1}^3 \cos\left(p\theta_r - \frac{2(j-1)\pi}{3}\right) \cdot i_{js} \end{aligned} \tag{XLII}$$

or in a more compact general form, using (XVII), as

$$\Gamma_e(\mathbf{I}_s, \theta_r) = \mathbf{I}_s^T \frac{d}{d\theta_r} \{\Lambda_{sm}(\theta_r)\} = \frac{1}{L_s} \Lambda_{ss}^T(\mathbf{I}, \theta_r) \frac{d}{d\theta_r} \{\Lambda_{sm}(\theta_r)\} \tag{XLIII}$$

The first two terms in (XL), which vanish in (XLII), represent the reluctance torque that tends to align the salient poles in the minimum reluctance position with rotating air gap flux. Motor torque control in high performance industrial drives is achieved by an electronically commutated 3-phase PWM inverter which forces the armature phase currents i_{js} in (XLII) to follow the sinusoidal reference currents i_{dj} generated from a prescribed torque demand signal $i/p \Gamma_d$ using rotor position information θ_r . In the 3Φ commutated BLMD system in Figure 1A the reference sinusoids, issued from the phase generator, are amplitude modulated (AM) by the i/p torque demand Γ_d or velocity error signal via a multiplying DAC. This AM effect is reflected in winding current amplitudes I_{jm} which vary with time as $I_{jm}(t)$ in symphony with the current demand signals $\{I_{dar}, I_{dbr}, I_{dc}\}$. These winding currents can be thus written in the following vector form, with amplitude variation included, as

$$\mathbf{I}_s(t) = \begin{bmatrix} i_{1s} \\ i_{2s} \\ i_{3s} \end{bmatrix} = \begin{bmatrix} I_{1m}(t) \cos(\omega_e t) \\ I_{2m}(t) \cos(\omega_e t - \frac{2\pi}{3}) \\ I_{3m}(t) \cos(\omega_e t + \frac{2\pi}{3}) \end{bmatrix} \tag{XLIV}$$

Consequently the developed torque is expressed by (XLII) in its most general form to allow for current amplitude variations which track the i/p torque demand signal excursions during transient step changes. Expression (XLII) is employed during BLMD model simulation to compute the motor torque from the derived stator winding currents for simulation of the rotor shaft drive dynamics. The steady state motor torque is determined from (XLIII), for balanced 3Φ phase conditions with constant amplitude stator winding currents as in (III), with

$$\Gamma_e(\mathbf{I}_s, \theta_r) = K_e I_m \sum_{j=1}^3 \cos\left(p\theta_r - \frac{2(j-1)\pi}{3}\right)^2 = \frac{3}{2} I_m K_e \tag{XLV}$$

The mechanical power P_m delivered by the magnetic coupling field can be determined from the applied motor torque in (XLII) which holds the rotor drive shaft load at an angular velocity ω_r as

$$P_m = \Gamma_e \omega_r = K_e \omega_r \sum_{j=1}^3 \cos\left(p\theta_r - \frac{2(j-1)\pi}{3}\right) \cdot i_{js} \tag{XLVI}$$

This is identical to electrical power P_e provided to each of the stator phase windings ignoring losses, by the PSU, in sustaining the magnetic coupling field from collapse during mechanical energy transfer. The electric power is accomplished by means of phase current i_{js} injection against coupling field back-emf reaction v_{ej} . The PSU contribution P_e is expressed by means of (XIV) and (XLIV) as $V_e^T I_s$ with

$$P_e = P_m = K_e \omega_r \sum_{j=1}^3 \cos(p\theta_r - \frac{2(j-1)\pi}{3}) i_{js} \tag{XLVII}$$

which defaults to (XLVI) for zero internal power factor angle φ_1 in the phasor diagram of Figure 10 and for constant amplitude winding currents.

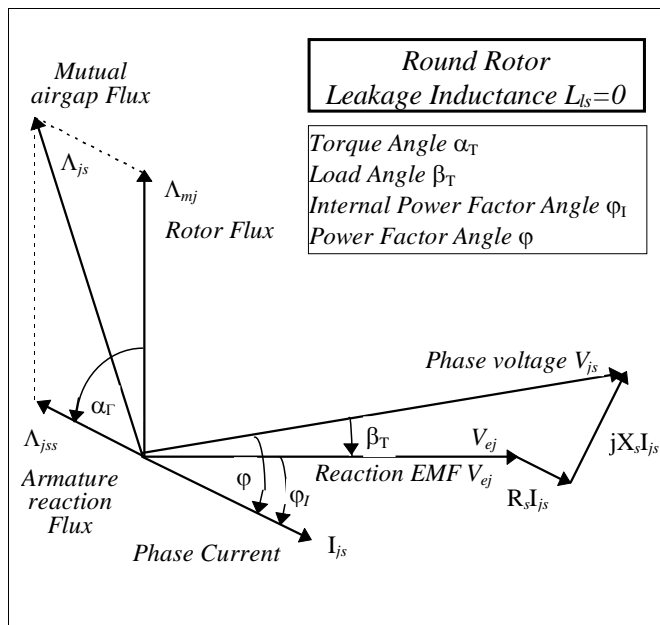


Fig. 10. Phasor diagram for PM motor

The physical manifestation of motor torque production, which is expressed as the product of stator current and the rotor air gap flux given in (XLIII), results from a tendency of the stator and rotor air gap flux fields to align their magnetic axes with minimum energy configuration. Consequently maximum torque is developed by the motor as in (XLIII) when the torque angle α_r , defined as the angle between the armature reaction $\Lambda_{ss}(I, \theta_r)$ and PM flux $\Lambda_{sm}(\theta_r)$ space vectors in (XVII), is maintained at 90 degrees. Optimum torque angle control can be achieved in a BLMD system by means of self synchronization, via a rotor shaft position resolver as shown in Figure 1, in which a current controlled PWM inverter ensures an orthogonal spatial relationship between the stator and rotor flux vectors. This can be visualized with the aid of the phasor diagram in Figure 10 where the torque angle α_r , given by

$$\alpha_r = \pi / 2 - \varphi_1 \tag{XLVIII}$$

with internal power factor angle ϕ_1 for steady state conditions, is forced towards 90 degrees by adjustment of the armature reaction field Λ_{jss} . This adjustment is accomplished with stator phase current I_{js} angle control, via electronic commutation, which also implies that the internal power factor angle ϕ_1 between the reaction EMF V_e and armature current I_s in (XLVII) is held at zero.

The PM air gap flux Λ_{mj} generates a phase-j reaction EMF V_{ej} in Figure 10 at steady state rotor angular velocity ω_r . This EMF has a maximum value for a given shaft speed when the phase winding axis is displaced 90 electrical degrees relative to the rotor flux axis in which case the phase winding conductors are opposite the rotor magnetic poles with zero flux linkage. Consequently the emf phasor V_{ej} lags the flux phasor Λ_{mj} by 90 degrees. The developed EM torque Γ_e results in sustained mechanical motion of motor drive shaft against a coupled load torque Γ_l , with angular velocity ω_r , expressed by the torque balance differential equation as

$$\Gamma_e - \Gamma_l = (J_m + J_l) \frac{d\omega_r}{dt} + B_m \omega_r \quad (\text{IL})$$

where J_m and J_l are the respective shaft and load moments of inertia and B_m is the motor shaft friction or damping coefficient. The motor shaft position θ_r is obtained from the rotor angular velocity by numerical integration during BLMD model simulation using

$$\theta_r = \int_0^t \omega_r(\xi) d\xi \quad (\text{L})$$

The equations (XXIII) and (XXIV) governing the electrical behaviour and the dynamical expressions (XXXII), (IL) and (L), together with the Laplace transform, form the basis of a mathematical model shown in Figure 1 of a brushless dc motor for complete simulation of the drive system.

2.2.4 Modelling of BLMD power converter with inverter blanking

Brushless motor speed or torque control is achieved by adjusting the amplitude and frequency of the stator winding phase voltages which are synchronized in phase with instantaneous rotor position. Several different methods of power converter operation in regulating the 3-phase motor winding voltage excitation have been reported in the literature (Murphy et al, 1989). The widely used method of ASD stator winding voltage control which relies on three-phase six-step inverter operation, with a basic 60 degree commutation interval over a 120 degree conduction mode and an adjustable dc link voltage, suffers from low order harmonics with resultant low speed motor torque pulsations (Jahns, 1984). An effective alternative to the six-step mode of operation relies on voltage control within the inverter using pulsewidth modulation. The PWM control strategy results in better overall transient response with the elimination of low frequency harmonic content and motor cogging if a large carrier to reference frequency ratio is employed. A wide variety of PWM techniques are available (Adams et al, 1975) such as synchronized square-wave (Pollack, 1972) and sinusoidal PWM (Grant et al, 1981, 1983) with the latter being the preferred choice in asynchronous form with a very large fixed carrier ratio in commercial applications. Smooth motor shaft rotation down to standstill is obtained via a sinusoidal asynchronous PWM inverter which delivers a high fidelity fundamental o/p voltage waveform to the stator windings. The accompanying distortion frequency components, due to modulated pulse shaping, are concentrated about the high frequency carrier and its harmonics and are easily attenuated by the stator winding inductances.

In a 3Φ current-controlled PWM inverter each current loop is equipped with a current controller and comparator modulator which provides wide bandwidth dynamic control of the stator current for high performance drive torque applications. Each current controller is fed with a sinusoidal current command reference i_{dj} from the 3Φ current commutator, shown in Figure 1, along with the sensed stator winding current feedback i_{fj} via Hall effect measuring devices. The rapidly adjusted error o/p $v_{cj}(t)$ from the current compensator forces the actual motor current i_{js} in each phase, via the high gain PWM controlled voltage-source inverter, to track the command reference in both phase and magnitude with minimal error.

A mathematical model of 3-phase inverter operation can be obtained by describing the control action of the pulsewidth modulator in each phase, fed with a fixed voltage dc supply U_d , on the amplitude and frequency adjustment of the BLMD stator winding voltage in response to the current compensator error output. Modulation proceeds in two steps in accordance with the current controller output as shown in Figure 1. A symmetrical double edge width modulated pulse train is generated for each phase by means of a voltage comparator as the first step. A triangular carrier waveform $V_{tri}(t)$, of fixed frequency f_s and common to all three phases, establishes the switching period T_s and the current control error reference $v_{cj}(t)$ then modulates the switch duty cycle as shown in Figure 11 for phase-a.

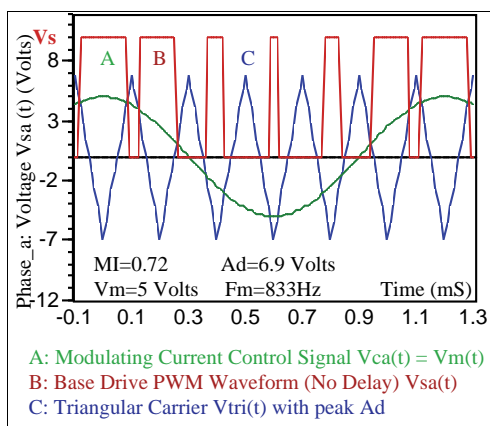


Fig. 11. Comparator modulator waveforms

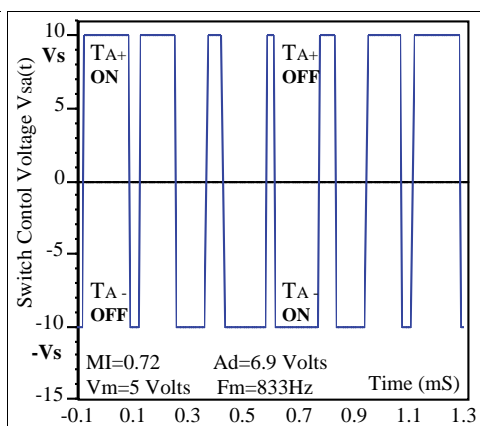


Fig. 12. Phase-a switch control voltage

The modulated bipolar switch pulse train $v_{sj}(t)$ is then used as the firing signal, at the modulator o/p as shown in Figure 12 for phase-a, to control the “ON” and “OFF” periods of the power transistors, via the base drive circuitry (BDA), in each half-bridge of the 3Φ inverter as the subsequent step. Similar switching sequences, with a phase angle separation of 120 degrees, are obtained for control of the other two phases of the inverter bridge resulting in a 3Φ PWM voltage supply to the motor stator windings. In practical inverters the finite turn-off time of the power transistor bridge necessitates the use of a finite blanking switch time in the PWM process to avoid short circuiting the dc busbar to ground (Murai, 1985; Evans et al, 1987; Dodson et al, 1990). This fixed ‘interlock delay’ δ , which is typically 20 μ S, is conservatively chosen for slow switching Darlington transistors in medium power motor drives in the low kilowatt range.

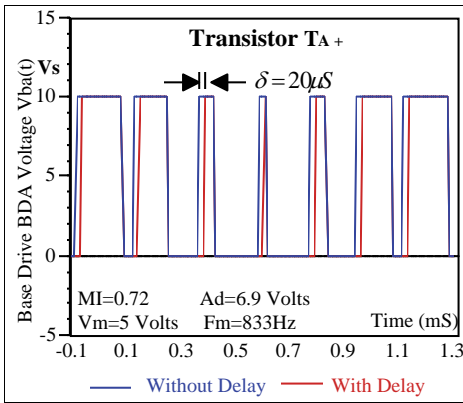


Fig. 13. Base drive voltage for TA+

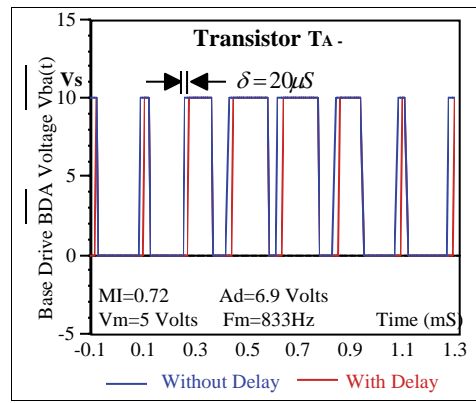


Fig. 14. Base drive voltage for TA-

This dwell time, between successive power transistor switching instants, is effected through an integrate and dump RC 'lockout' network connected to a voltage threshold in the base drive circuitry. A switching delay of this magnitude, for inverter frequencies in the audio range (5kHz), has to be included in the motor drive modelling process for accurate simulation studies. The effect of the switching delay can be modelled as follows by considering phase-a only with a similar procedure for the other two phases (Guinee et al, 1998, 1999).

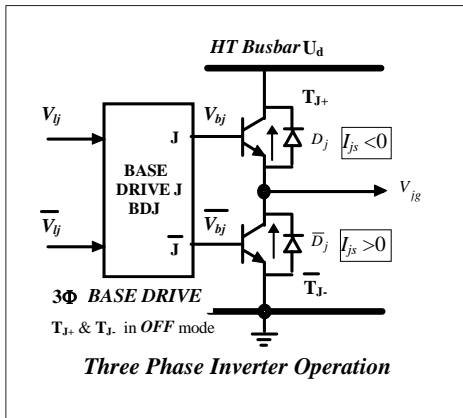


Fig. 15. Phase-j inverter operation

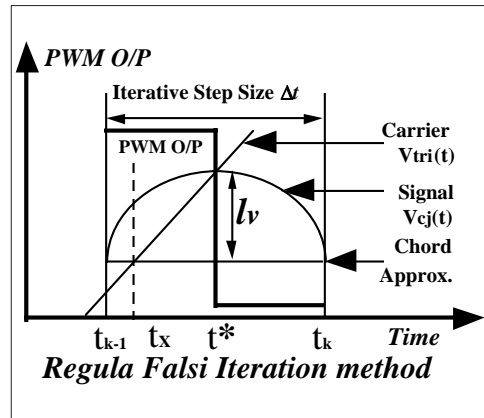


Fig. 16. Regula-falsi iterative search

The duty cycle of the bipolar switch control voltage $v_{sa}(t)$, during one switching period T_s in Figure 12 is determined by the relative magnitude comparison and accurate crossover evaluation, from simulation via the regula-falsi iterative search method shown in Figure 16, of the current control voltage $v_{ca}(t)$ with the dither reference $v_{tri}(t)$. The switch control pulse sequence can be described as

$$v_{sa}(t) = \begin{cases} +V_s & \{v_{ca}(t) \geq v_{tri}(t)\} \\ -V_s & \{v_{ca}(t) < v_{tri}(t)\} \end{cases} \quad (LI)$$

with modulated pulse duration

$$\tau = \begin{cases} T_s & \{v_{ca}(t) \geq A_d\} \\ (1 + m_f) \frac{T_s}{2} & \{|m_f| < 1\} \\ 0 & \{v_{ca}(t) \leq -A_d\} \end{cases} \quad (LII)$$

for carrier amplitude A_d and modulation index (MI) m_f given by

$$m_f = v_{ca}(t)/A_d \quad (LIII)$$

The effect of the switch control voltage on the inverter base drive transistors T_{A+} and T_{A-} under ideal conditions, without delay is illustrated in Figures 13 and 14.

When blanking is introduced inverter switching is postponed until the capacitor voltages of the complementary RC delay circuits, associated with power transistors T_{A+} and T_{A-} , exceeds the threshold level setting V_{th} in the base drivers as shown in Figures 13 and 14 and detailed in Figure 17. The magnitude of the delay δ , typically 20µS, is given by

$$\delta = RC \ln\left(\frac{2V_s}{V_s - V_{th}}\right) \approx 0.693RC \text{ if } V_{th} = 0 \quad (LIV)$$

When phase-a power transistors T_{A+} and T_{A-} , are "OFF" during the blanking period winding current conduction is maintained through free-wheeling protection diodes, as shown in Figures 1 and 15, so that each transistor with its accompanying antiparallel diode functions as a bilateral switch. The relationship between the states of the dc to ac converter phase-a switch transistor pair, denoted by $S_A(k)$ with $k \in \{0,1,2\}$, and the base drive voltages v_{la} & \bar{v}_{la} in Figure 17 can be represented by

$$\begin{aligned} S_A(0) &= \begin{cases} v_{la} < V_{th} \Rightarrow v_{ba}(t) = 0 \Rightarrow T_{A+} \text{ is "OFF"} \\ \bar{v}_{la} \geq V_{th} \Rightarrow \bar{v}_{ba}(t) = V_B \Rightarrow T_{A-} \text{ is "ON"} \end{cases} \\ S_A(1) &= \begin{cases} v_{la} \geq V_{th} \Rightarrow v_{ba}(t) = V_B \Rightarrow T_{A+} \text{ is "ON"} \\ \bar{v}_{la} < V_{th} \Rightarrow \bar{v}_{ba}(t) = 0 \Rightarrow T_{A-} \text{ is "OFF"} \end{cases} \\ S_A(2) &= \begin{cases} v_{la} < V_{th} \Rightarrow v_{ba}(t) = 0 \Rightarrow T_{A+} \text{ is "OFF"} \\ \bar{v}_{la} < V_{th} \Rightarrow \bar{v}_{ba}(t) = 0 \Rightarrow T_{A-} \text{ is "OFF"} \end{cases} \end{aligned} \quad (LV)$$

with similar expressions $S_J(k)$ and $J \in \{A,B,C\}$ for the other two phases. The power transistors in each leg of the inverter are thus alternately switched "ON" and "OFF" according to the tristate expression (LV) with a brief blanking period separating these switched transistor conduction states. The tristate operation of the power converter bridge also determines the phase potential i/p of the stator winding as a result of the PWM gating sequence applied to the basedrive in (LV). The corresponding converter voltages applied between the stator phase winding input connection and ground, denoted by v_{ag} , v_{bg} , and v_{cg} , are then given by

$$\begin{aligned}
 v_{ag} &= \begin{cases} U_d & \{S_A(1) \text{ or } S_A(2) \& i_{as} < 0\} \\ 0 & \{S_A(0) \text{ or } S_A(2) \& i_{as} > 0\} \end{cases} \\
 v_{bg} &= \begin{cases} U_d & \{S_B(1) \text{ or } S_B(2) \& i_{bs} < 0\} \\ 0 & \{S_B(0) \text{ or } S_B(2) \& i_{bs} > 0\} \end{cases} \\
 v_{cg} &= \begin{cases} U_d & \{S_C(1) \text{ or } S_C(2) \& i_{cs} < 0\} \\ 0 & \{S_C(0) \text{ or } S_C(2) \& i_{cs} > 0\} \end{cases}
 \end{aligned} \tag{LVI}$$

where current flow into a winding is assumed positive by convention. If the phase current flow i_{js} is positive in (LVI) during blanking when power transistors T_{j+} and T_{j-} are "OFF", as shown in Figure 15, then $v_{jg} = 0$. If, however, i_{js} is negative then $v_{jg} = U_d$ while T_{j+} and T_{j-} are blanked. The tristate operation of the inverter bridge also uniquely determines the phase potential i/p v_{jg} of the stator winding in (LVI) as a result of the PWM gating sequence applied to the basedrive in (LV). The inverter o/p voltage v_{ag} is shown in Figures 18 and 19 for the two cases of current flow direction in phase-a of the stator winding. The potential of the stator winding neutral star point s , from equation (XXIII) with phase current summation

$$\sum_{j=1}^3 i_{js} = i_{as} + i_{bs} + i_{cs} = 0 \tag{LVII}$$

is given by

$$v_{sg} = \frac{1}{3}(v_{ag} + v_{bg} + v_{cg}) \tag{LVIII}$$

with resultant phase voltages

$$\begin{aligned}
 v_{as} &= (v_{ag} - v_{sg}) = \frac{1}{3}(2v_{ag} - v_{bg} - v_{cg}) \\
 v_{bs} &= (v_{bg} - v_{sg}) = \frac{1}{3}(2v_{bg} - v_{ag} - v_{cg}) \\
 v_{cs} &= (v_{cg} - v_{sg}) = \frac{1}{3}(2v_{cg} - v_{ag} - v_{bg})
 \end{aligned} \tag{LIX}$$

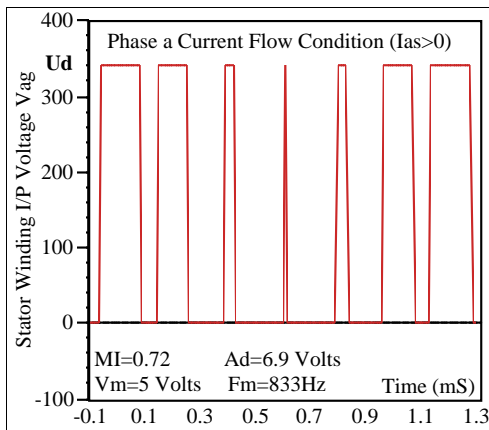


Fig. 18. Inverter o/p Voltage ($i_{as} > 0$)

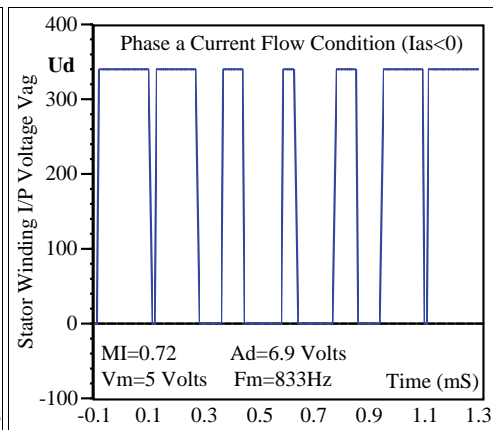


Fig. 19. Inverter o/p Voltage ($i_{as} < 0$)

The complete three phase model of a typical high performance servo-drive system (Moog GmbH, 1989; Guinee, 1999). incorporating equations (XXIII), (XXIV), (XLII), (IL), (L), (LV), (LVI) and (LX), used in software simulation for parameter identification purposes is displayed in Figure 17.

3. Numerical simulation accuracy and experimental validation of BLMD model

Since the BLMD model is partitioned into linear elements and non linear subsystems, owing to the complexity and discrete temporal nature of the PWM control switching process, numerical integration techniques have to be applied to obtain solutions to the differential electrodynamic equations of motion. Numerical simulation of the continuous-time subsystems, with a transfer function representation based on the Laplace transform, is achieved by means of model difference equations with numerical solutions provided by the use of the backward Euler integration rule (BEIR) (Franklin et al, 1980). In this instance continuous time derivatives are approximated in discrete form using the Z Transform substitution operator $S = \frac{1}{T}(1 - Z^{-1})$. Since the BEIR maps the left half s-plane inside the unit circle in the z-plane these solutions are stable. The choice of this implicit integration algorithm is based on its simplicity of substitution, ease of manipulation with a small number of terms and reduced computation effort in the overall complex BLMD model simulation. An alternative filter discretization process based on Tustin's bilinear method, or the trapezoidal integration rule with the substitution operation $S = \frac{2}{T}(1 - Z^{-1}) / (1 + Z^{-1})$, can be implemented with negligible observable differences at the small value of integration step size T actually chosen. The application of the BEIR technique can be visualized for a first order system, as in the case of the current control lag compensator G_I which has a generalized transfer function (Guinee, 2003)

$$G_I(s) = \frac{V(s)}{I(s)} = K_c \frac{1 + \tau_p s}{1 + \tau_b s} \equiv K \frac{\alpha_0 + \alpha_1 s}{\beta_0 + \beta_1 s} \quad (\text{LX})$$

with continuous-time description given by

$$\beta_0 V(t) + \beta_1 \frac{dV(t)}{dt} = K \left(\alpha_0 I(t) + \alpha_1 \frac{dI(t)}{dt} \right) \quad (\text{LXI})$$

Integrating (LXI) between the discrete time instants t_k and t_{k-1} with a fixed time step size T gives

$$\beta_1 V(t_k) - K \alpha_1 I(t_k) = [\beta_1 V(t_{k-1}) - K \alpha_1 I(t_{k-1})] + K \alpha_0 \int_{t_{k-1}}^{t_k} I(\tau) d\tau - \beta_0 \int_{t_{k-1}}^{t_k} V(\tau) d\tau \quad (\text{LXII})$$

Applying the BEIR, with piecewise constant integrand backward approximations $V(t_k)$ and $I(t_k)$ over the interval $t_k \geq t > t_{k-1}$ yields the input-output difference equation

$$V(t_k) [\beta_1 + \beta_0 T] = \beta_1 V(t_{k-1}) + K [\alpha_1 + \alpha_0 T] I(t_k) - K \alpha_1 I(t_{k-1}) \quad (\text{LXIII})$$

This can be expressed in the Z domain, via the Z Transform, as the transfer function

$$\frac{V(Z)}{I(Z)} = K \frac{\alpha_0 + \alpha_1 \frac{1}{T}(1 - Z^{-1})}{\beta_0 + \beta_1 \frac{1}{T}(1 - Z^{-1})} \equiv k \frac{n_0 + n_1 Z^{-1}}{d_0 + d_1 Z^{-1}} \quad (\text{LXIV})$$

which is equivalent to (LX) through the general BEIR substitution operator $S = \frac{1}{T}(1 - Z^{-1})$. The time evolution of each discretized linear subsystem proceeds according to the BEIR, similar to (LXIII), as an integral part of the overall BLMD numerical simulation with a fixed time step $T = \Delta t$ and input $x(t)$ to output $y(t)$ relationship given by

$$y^k = (n_0 x^k + n_1 x^{k-1}) \frac{k}{d_0} - \frac{d_1}{d_0} y^{k-1} \tag{LXV}$$

The choice of time step size is determined by the resolution accuracy of the PWM switching instants required during simulation for delayed inverter trigger operation as explained in section 3.1 below. The BLMD model program is organized into a sequence of software function calls, representing the operation of the various subsystems.

3.1 PWM simulation with inverter delay

The choice of numerical integration step size Δt , for solution of the set of dynamic system differential equations, is influenced by the PWM switching period T_s ($\approx 200\mu\text{s}$) (Moog, 1989) and the smallest BLMD time constant τ_d ($\approx 28.6\mu\text{s}$) associated with the basedrive 'lockout' circuitry. Furthermore the precision with which the pulse edge transitions are resolved in the three phase PWM o/p sequences as in (LI) with inverter blanking included, has a significant effect on the accuracy of the inverter o/p waveforms. This is important in BLMD simulation where model accuracy and fidelity are an issue in dynamical parameter identification for optimal control. The effect of inaccuracy in pulse time simulation can be reduced by choosing a sufficiently small fixed time step $\Delta t \ll T_s$, such as $0.5\%T_s$ or 5% of the inverter dead time δ ($\approx 20\mu\text{s}$) for example, to reflect overall BLMD model accuracy and curtail computational effort in terms of time during lengthy simulation trial runs. Furthermore this choice of step size also provides an uncertainty bound of $+\Delta t$ in the evaluation of PWM switching instants during simulation in the absence of an iterative search of the switch crossover time. This uncertainty can be reduced by an iterative search of the PWM crossover time t^* within a fixed assigned time step size Δt during BLMD simulation for which a width modulated pulse transition has been flagged as shown in Figure 16. A variety of iterative search methods can be employed for this purpose with varying degrees of computation runtime required and complexity. These include, for example, successive application of the bisection method, regula falsi technique and the Newton-Raphson approach (Press et al, 1990) where convergence difficulties can arise with derivative calculations from noisy current control signals. The number of iterations n required for the bisection technique, with a fixed time step Δt , to reach an uncertainty ε in the pulse transition time estimate t_X , is given by the error criterion

$$\Delta t 2^{-(n+1)} \leq \varepsilon \tag{LXVI}$$

The estimate of the PWM switching time t^* obtained via the regula falsi method, from the comparison of the triangular carrier ramp with the piecewise linear approximation of the control signal v_{cj} as shown in Figure 16, is given by the iterative search value t_X as (Guinee, 1998, 2003)

$$t_X = \frac{\{v_{ri}(t_{k-1}) - v_{cj}(t_{k-1})\} \Delta t}{\{v_{ri}(t_{k-1}) - v_{cj}(t_{k-1})\} - \{v_{ri}(t_k) - v_{cj}(t_k)\}} + t_{k-1} \tag{LXVII}$$

The adoption of a single iteration of the regula falsi method along with a small simulation time step Δt simplifies the search problem of the pulse edge transition with sufficient accuracy without the expenditure of considerable computational effort for a modest gain in accuracy by comparison with the other iterative methods available. An indication of the step size required for accurate resolution of PWM inverter operation with delay can be obtained from consideration of the anticipated signal ‘curvature’ due to (a) the signal bandwidth and amplitude at the current controller o/p v_{cj} in the magnitude comparison with the triangular carrier shown in Figure 16 in the comparator modulator and (b) the rate of exponential voltage ramp up to the base drive threshold V_{th} , which controls the inverter dead time, in the RC delay circuits shown in Figure 20.

The maximum harmonic o/p voltage from the high gain current compensator G_I is determined by the carrier amplitude A_d at the onset of overmodulation ($m_f = 1$) in PWM inverter control with a frequency that is limited by the 3dB bandwidth $\omega_F = 1/\tau_F$ ($\sim 3\text{kHz}$ in Table I) of the smoothing filter H_{FI} in the current loop feedback path shown in Figure 17. This may be represented in analytic form as

$$v_{cj}(t) = A_d \sin(\omega_F t) \tag{LXVIII}$$

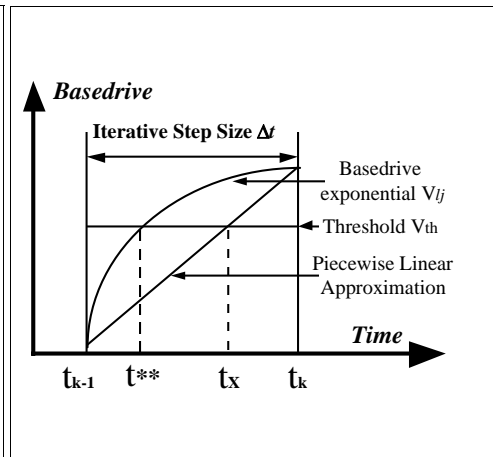
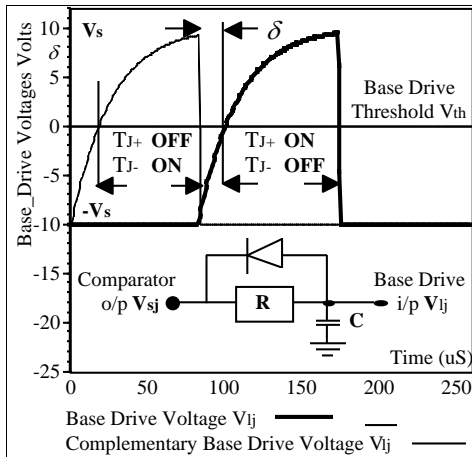


Fig. 20. Delayed basedrive trigger signals

Fig. 21. Basedrive Trigger Time Search

with a quadratic power series approximation about the mid interval point \hat{t} in Δt given by

$$v_{cj}(t) = v_{cj}(\hat{t}) + v'_{cj}(\hat{t})(t - \hat{t}) + \frac{v''_{cj}(\hat{t})}{2!}(t - \hat{t})^2 . \tag{LXIX}$$

The accuracy with which the estimated width modulated pulse transition instants t_x are determined can be gauged by comparing the deviation error of the actual intersection time t^* of the triangular carrier with the control signal v_{cj} , due to its curvature, to that t_x obtained with the piecewise linear chord approximation of the signal in the regula-falsi method as illustrated in Figure 16. The ‘curvature’ of the signal in (LXVIII) with time, determined (Kreyszig, 1972) from

$$\kappa = \left| \frac{v''_{cj}}{1 + v'^2_{cj}} \right| , \tag{LXX}$$

is given by its maximum value

$$\kappa_{\max} = |v_{cj}''| = A_d \omega_F^2 \tag{LXXI}$$

at the peak amplitude A_d of $v_{cj}(t)$ corresponding to the instant $t^* = \pi/2\omega_F$ in Figure 16 at which $v_{cj}'(t^*) = A_d \omega_F \cos(\omega_F t^*) = 0$. The peak deviation l_v of the signal due to curvature from the chord approximation through t_{k-1} in Figure 16 occurs at $\hat{t} = t^*$ with zero chord slope. The peak deviation from the chord, through $t_{k-1} = (t^* - \Delta t/2)$, is determined by the Taylor series expansion in (LXIX) about $\hat{t} = t^*$ with

$$v_{cj}(t_{k-1}) = v_{cj}(t^*) + \frac{v_{cj}''(t^*)}{2!} \left(\frac{\Delta t}{2}\right)^2 = A_d \left[1 - \frac{1}{2} \left(\frac{\omega_F \Delta t}{2}\right)^2 \right] \tag{LXXII}$$

giving

$$l_v = [v_{cj}(t^*) - v_{cj}(t_{k-1})] = \frac{A_d}{2} \left(\frac{\omega_F \Delta t}{2}\right)^2 \tag{LXXIII}$$

The worst case deviation error of the pulse transition time estimate t_x from t^* is determined by the regula-falsi method at the point of intersection t_x of the carrier ramp, which passes through the signal coordinates $[t^*, v_{cj}(t^*)]$ in Figure 16, with the chord approximation to the signal. The approximation error ($t^* - t_x$) is determined from the ramp, which has peak-to-peak excursion $2A_d$ over the half period $T_s/2$, with slope $m = 4A_d/T_s$ as

$$\varepsilon = (t^* - t_x) = \left(\frac{l_v}{m}\right) = \left(\frac{T_s}{8}\right) \cdot \left(\frac{\omega_F \Delta t}{2}\right)^2 \tag{LXXIV}$$

Substitution of the set of relevant signal parameters $\{T_s, A_d, f_F\}$, for a step size of $1\mu s$, with values $\{200 \mu s, 6.9V, 3kHz\}$ result in a negligible approximation error ε relative to the step size Δt of 0.222% which verifies the suitability of the chosen step size for a linear search of the PWM crossover time. The PWM resolution accuracy determines the moment that a modulated pulse edge transition takes place with subsequent onset of inverter blanking, using lockout circuitry, which substantially affects power transfer from the dc supply to the prime mover. The next essential trigger event, that needs to be accurately resolved, is the instant at which retarded firing of the inverter power transistors commences when the RC delay growth voltage exceeds the basedrive threshold $V_{th} = 0$ in Figure 20. The complementary exponential trigger voltages v_{ij} & \bar{v}_{ij} supplied to the basedrive circuitry, for a modulator peak-to-peak o/p swing of $2V_s$, can be expressed as

$$v_{ij} = V_s(1 - 2e^{-t/RC}) \tag{LXXV}$$

The basedrive turnon time t^{**} is given by (LIV) as δ ($\sim 19.82\mu s$), at the instant at which $v_{ij}(t^{**}) = V_{th}$, for a time constant τ_d ($\sim 28.6\mu s$). Since delay circuit simulation is employed the trigger instant t_x has to be obtained using piecewise linear approximation of the exponential growth waveform, within the flagged simulation interval as shown in Figure 21, and is given by

$$t_x = t_{k-1} - \frac{v_{ij}(t_{k-1})}{v_{ij}(t_k) - v_{ij}(t_{k-1})} \Delta t \tag{LXXVI}$$

where $t_{k-1} < t_x < t_k$ and $t_{k-1} < t^{**} < t_k$. Assume that t^{**} occurs at the mid interval time $(t_{k-1} + \Delta t/2)$ which thus provides an absolute point of reference for comparison with the search estimate t_x . The effect of basedrive signal 'curvature' on the trigger estimate t_x can be gauged by monitoring the relative contribution of the quadratic terms in the Taylor series expansion about t^{**} as

$$v_{ij}(t_x) = v_{ij}(t^{**}) + v'_{ij}(t^{**})(t_x - t^{**}) + \frac{v''_{ij}(t^{**})}{2!}(t_x - t^{**})^2 \quad (\text{LXXVII})$$

with $v_{ij}(t^{**}) = V_{th} = 0$. The differential error ε in the crossover time estimate in (LXXVI) is given by

$$\varepsilon = (t_x - t^{**}) = \left[\frac{e^{\frac{\Delta t}{2RC}} - 1}{\frac{\Delta t}{e^{2RC} - e} - \frac{\Delta t}{2RC}} - \frac{1}{2} \right] \Delta t \approx 4.37 \times 10^{-3} \Delta t \quad (\text{LXXVIII})$$

and is practically zero for very small time steps which implies a negligible quadratic contribution. Consequently the trigger time estimate obtained by linear approximation of the basedrive voltage about the threshold is very accurate for the time step size chosen.

3.2 Motor dynamic testing and simulation

The steady state controlled torque versus output speed characteristic (Moog, 1988) for the particular motor drive concerned is almost constant over a 4000 rpm speed range for a rated continuous power o/p of 1.5kW. The corresponding dynamic transfer characteristic of o/p motor torque Γ_e versus input torque demand Γ_d voltage is practically linear in the range (0, ± 10) volts. A fixed step signal Γ_d i/p is chosen to provide persistent excitation, as a standard control stimulus for dynamic system response testing, and in particular to gauge the accuracy of the model simulation and parameter extraction process based on the feedback current (FC) response i_{ij} . This response has the transient features of a constant amplitude swept frequency sinusoid, during the acceleration phase of the motor shaft, which are beneficial for test purposes and BLMD model validation in system identification (SI). The phase current feedback simulation can then be checked against experimental test results as the observed target data, for example in phase-a, for both phase and frequency coherence in model validation. Further model validation is provided by the accuracy with which high frequency ripple in the unfiltered current feedback is replicated through BLMD simulation when compared with experimental test data. Examination of the presence of dead time related low frequency harmonics in the simulated current feedback is also used to gauge BLMD model fidelity, through FFT spectral analysis, when compared with measurement data. An input magnitude of 1volt is sufficient to guarantee linear operation and avoid saturation ($m_f > 1$) of the PWM stage by the high gain current controller chosen here as the optimizer module MCO 402B in Table 1. This input step size is also enough to slow down the rate of shaft speed ramp up to allow adequate resolution of the frequency change in the FC target data.

The intrinsic mechanical parameters of motor viscous friction B_m and shaft inertia J_m are initially determined from experimental motor testing and cost surface simulations based on the mean squared error (MSE) between the simulated and measured transient response data for shaft velocity and current feedback. Two examples of known shaft load inertia J_L are

then used in simulated response measurements as a check against BLMD test data for further model accuracy and validation. These simulation results, which correspond to the different inertial loads, are integrated into a parameter identification process, using MSE cost surface simulation, based on a Fast Simulated Diffusion (FSD) optimization technique for the purpose of motor drive shaft parameter extraction. The experimentally determined parameter values listed in Table II for the BLMD model are used in all model simulations. The back EMF or voltage constant K_e was experimentally determined from an open circuit (o/c) test with the motor configured as a generator driven over a range of speeds by an identical shaft coupled BLMD system. The generator voltage characteristic V_g is linear with drive shaft speed ω_m as shown for the experimental data in Figure 22, according to (XXIV), with slope K_e derived from the fitted linear voltage relationship V_f . The transducer velocity 'gain' G_{RDC} of the Resolver-to-Digital Converter (RDC) was concurrently estimated along with K_e from the slope of the fitted linear characteristic $V_{f\omega}$ which in addition substantiates the converter linearity, to the speed voltage measurements shown in Figure 23. This value along with the cascaded shaft velocity filter gain is given as the cumulative gain H_{v0} in Table II.

Torque Demand Filter H_T	$K_T=1.0; \tau_T=222\mu S$	Voltages	$U_d=310$ Volts; $V_{th}=0$; $V_S=10$ Volts
Current Demand Filter H_{DI}	$K_I=1.0; \tau_I=100\mu S$	Constants	$K_{wi}=6.8 \times 10^{-2}$; $K_e = K_f = 0.3$
Current Feedback Filter H_{FI}	$K_F=5.0; \tau_I=47\mu S$	Winding	$P=6$; $r_S=0.75$ Ohms; $L_S=1.94$ mH
Basedrive Delay Circuit	RC =28.6 μS	Carrier	$f_s=5$ kHz; $A_d=6.9$ Volts;
Current Controller Type High Gain: MCO 402B Low Gain: MCO 422	$K_C=19.5$; $\tau_a=225\mu s$; $\tau_b=1.5$ ms $K_C=5.0$; $\tau_a=223\mu S$; $\tau_b=0.7$ mS	Motor Dynamics	$J_m=3$ kg.cm ² ; $B_m=2.14 \times 10^{-3}$ Nm.rad ⁻¹ .sec
Shaft Velocity Filter H_V	$H_{v0}=13.5 \times 10^{-3}$; $\alpha=\sqrt{2}$; $\omega_0=2 \times 10^3$ rad.sec ⁻¹	Inertial Loads	$J_{MML}=9.06$ kg.cm ² (Medium Mass -MML) * $J_{LML}=17.8$ kg.cm ² (Large Mass - LML)
*Returned Parameter Estimates: $\hat{J}_{opt} = J_m + \hat{J}_{LML} = 20.838$ kg.cm ² , $\hat{B}_{opt} = 1.959 \times 10^{-3}$ Nm.Sec.Rad ⁻¹			
* Simulated FC Response Surface Estimates: $J_{opt}=20.877$ kg.cm ² , $B_{opt}=1.921 \times 10$ Nm.Sec.Rad ⁻¹			

Table II. BLMD system parameters

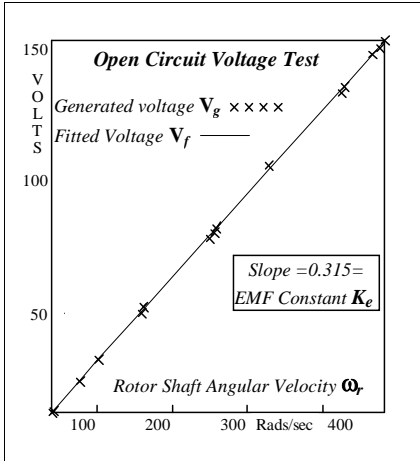


Fig. 22. Estimation of EMF constant K_e

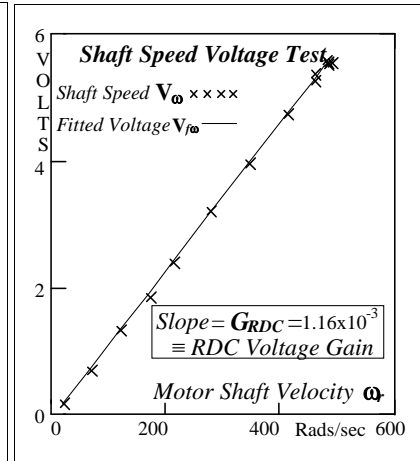


Fig. 23. Estimation of RDC 'gain' G_{RDC}

The value of K_e was subsequently used in a motor-generator electrical load test, at different speeds as illustrated in Figure 24, to estimate the stator winding parameters L_s and r_s as a cross check of the nominal catalogued (Moog, 1998) values. The difference ΔV between the measured terminal voltage V_T , across the load resistance R_L and the generated voltage V_G using the fitted coefficient K_e via (XXIV) is equated to the internal voltage drop of the Thevenin equivalent circuit shown in Figure 24 with

$$\Delta V = V_G - V_T = |Z| I_L \tag{LXXIX}$$

where

$$I_L = V_T / R_L.$$

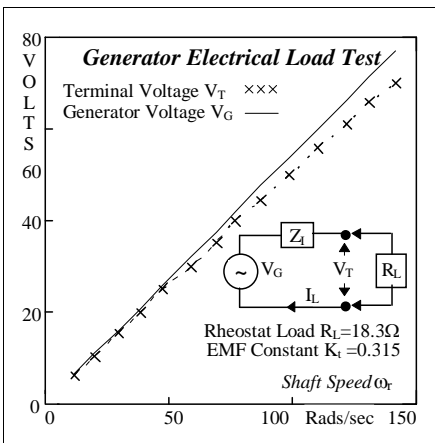


Fig. 24. Motor - generator load test

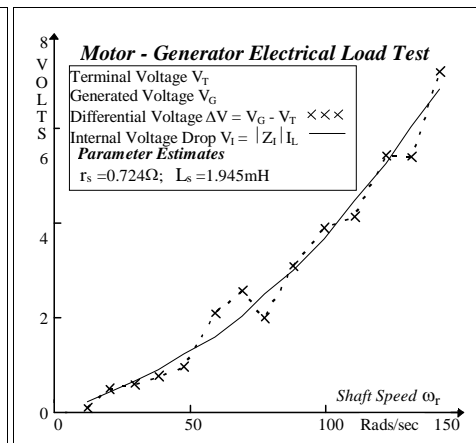


Fig. 25. Winding parameter estimation

The quadratic polynomial expressed in terms of ω_e via the circuit parameters as

$$Z^2 = a_0 + b_0 \omega_e^2 \tag{LXXX}$$

for $\omega_e = p\omega_r$ and constant coefficients $a_0 \equiv r_s^2$ and $b_0 \equiv L_s^2$, is fitted to the derived data $y = (\Delta V/I_L)^2$. The quadratic fit shown in Figure 25 is based on the minimization of the MSE (E), between the sampled y_k and simulated Z_k^2 data, as

$$E = \frac{1}{N} \sum_{k=1}^N [y_k - a_0 - b_0 x_k^2]^2 \text{ for } x = \omega_e \tag{LXXXI}$$

with respect to a_0 and b_0 . The cost function minimisation results in the normal equations

$$b_0 = \frac{\sum_k x_k^2 \sum_k y_k - N Y^T X^2}{(\sum_k x_k^2)^2 - (X^2)^T X^2} \tag{LXXXII}$$

$$a_0 = \frac{1}{N} \left[\sum_k y_k - b_0 \sum_k x_k^2 \right] \tag{LXXXIII}$$

with parameter estimates $\hat{L}_s = 1.945\text{mH}$ and $\hat{r}_s = 0.724$ ohms that are very close to the nominal values in Table II.

The motor shaft friction coefficient B_m was obtained from the steady state current feedback I_{fa} in phase-a at various shaft speeds ω_r by means of the torque constant K_t which is numerically equal to the experimentally determined value of K_e when proper units are used. The active component of the steady state current feedback is considered in the calculation of the dissipative friction torque by allowing for the effect of the machine impedance angle φ_z increase, given by

$$\varphi_z = \text{Tan}^{-1} \left(\frac{X_s I_{js}}{r_s I_{js}} \right) = \text{Tan}^{-1} \left(\frac{p\omega_r L_s}{r_s} \right), \tag{LXXXIV}$$

with motor shaft speed and zero load angle β_T in Figure 10. This is necessary in electronic commutated motor drive systems, in which the current controlled applied phase voltage v_{js} at zero load angle is derived from the current demand I_{dj} in Figure 17, without the benefits of adaptive current angle advancement (Meshkat, 1985) to counteract the torque reduction effects of internal power factor angle illustrated in Figure 10. The derived friction torque, from the adjusted measured current feedback $I_{fa} \cos \varphi_z$, is given by

$$\Gamma_f = \left(\frac{3}{2}\right) K_t I_{as} \cos \varphi_z = \left(\frac{3}{2}\right) \left(\frac{K_t}{K_{wi} K_f}\right) I_{fa} \cos \varphi_z \tag{LXXXV}$$

via (XLV) for balanced 3-phase conditions where the current feedback factor K_{wi} and filter gain K_f are considered in the estimation of the stator current flow I_{js} . This is graphed in Figure 26 for the measured FC test data I_{fa} and equated to the steady state mechanical friction torque via (II) as

$$\Gamma_f = B_m \omega_r. \tag{LXXXVI}$$

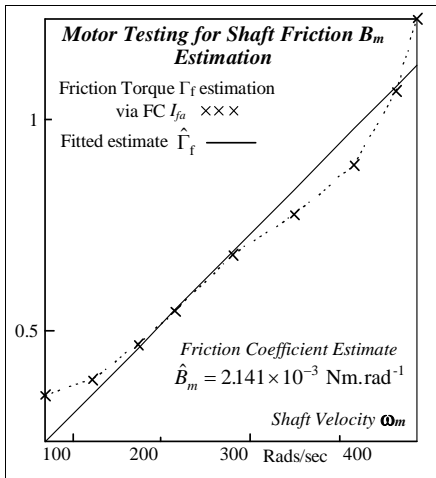


Fig. 26. Friction parameter estimation

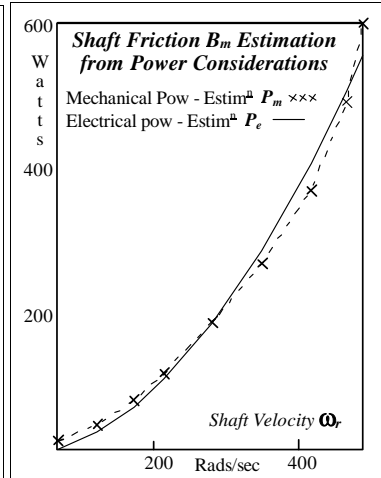


Fig. 27. Friction power estimation

The friction coefficient B_m is obtained from a linear first order polynomial fit, displayed in Figure 26, based on expression (LXXXVI) with estimate $\hat{B}_m = 2.141 \times 10^{-3} \text{ Nm.rad}^{-1}$ as in Table II. Alternative confirmation of the accuracy of the damping factor estimate is obtained from consideration of the electrical power transfer P_e from the coupling field expressed in (XLVII) and comparison with the resultant mechanical power dissipation P_m associated with dynamic friction via (XLVI). The continuous power supplied from the coupling field, necessary to sustain motor rotation with frictional losses at various shaft speeds under steady state conditions, is determined from the rms values of reaction EMF using the measured estimate \hat{K}_e from the o/c test and the experimental FC test data with lagging power factor balanced over three phases as

$$P_e = 3 \left(\frac{I_{fa}}{\sqrt{2} K_m K_f} \cos \varphi_z \right) \left(\frac{\hat{K}_e \omega_r}{\sqrt{2}} \right). \tag{LXXXVII}$$

The mechanical power dissipated as frictional heat is evaluated from (LXXVI) using the measured estimate \hat{B}_m as

$$P_m = \Gamma_f \omega_r = \hat{B}_m \omega_r^2 \tag{LXXXVIII}$$

Both power estimates exhibit a high degree of correlation, with correlation coefficient ρ (Bulmer, 1979) of 99.5%, when plotted in Figure 27 which validates the derived damping factor estimate \hat{B}_m .

3.3 Motor step response testing and simulation results

Synchronized initial conditions for BLMD testing, and resultant comparison with model numerical simulation, are obtained by hand cranking the motor shaft to top dead centre of the phase-a current commutation reference position while monitoring the phase generator o/p waveforms before application of the torque demand step i/p. This is essential for

proper datum time referencing of all waveforms in the eventual comparison process, when formulating a multim minima cost surface for minimization purposes using the least squares error criterion, during parameter identification.

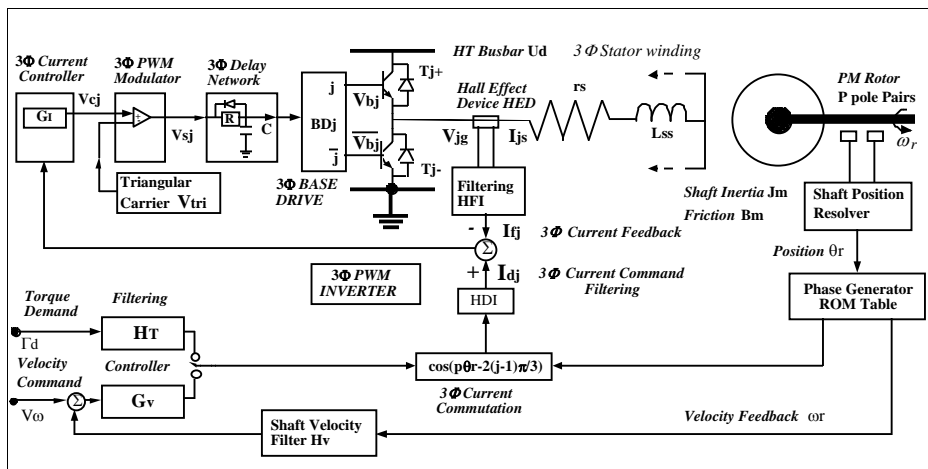


Fig. 28. Network structure of a typical BLMD system

The actual drive system with network structure as shown in Figure 28 was tested at critical internal nodes with multiplexed sampled data waveforms acquired at rates corresponding to the different inertial loaded shaft conditions (J_L) specified in Table III. The length of each data record is fixed at 4095 sample points with a normalized duration of approximately 10 machine FC cycles for reference purposes during comparison with simulated motor response for model validation and accuracy and also during system identification for accurate extraction of drive motor model parameter estimates.

FC Target Data	No Shaft Load (NSL)	Medium Inertial Load (MML)	Large Inertial Load (LML)
No. of machine cycles	~ 9.75	~ 11.5	~ 10.5
Acquisition rate T	20µs	40µs	49.6µs
No. of data points N_d	4095	4095	4095
Simulation time step	1µs	1µs	1µs
Decimation Factor	20	40	50
Waveform Correlation Analysis for BLMD system without inertial shaft loads			
Signal x	$Exp\ i_{xa}$	$Sim\ i_{xa}$	Data Correlation Coefficient ρ
Current Feedback	Fig. 29: I_{fa}	i_{fa}	0.985
Current Demand	Fig. 30: I_{da}	i_{da}	0.993
Current Controller o/p	Fig. 31: V_{ca}	v_{ca}	0.98
Motor Shaft Velocity	Fig. 32: $V_{\omega r}$	$v_{\omega r}$	0.98

Table III. Brushless Motor Drive Test and Simulation Results

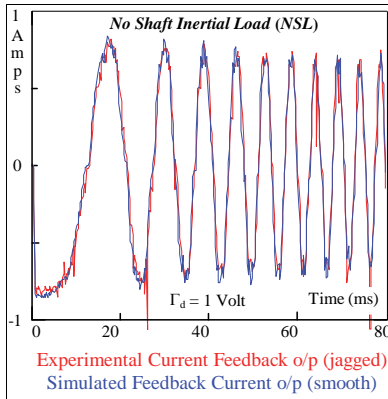


Fig. 29. BLMD current feedback I_{fa}

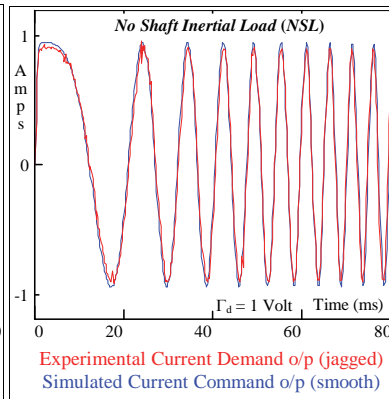


Fig. 30. BLMD current demand I_{da}

Verification of numerical simulation accuracy and BLMD model validation are immediately established by comparing the simulated step response characteristics with the actual test data in Figures 29 to 32 in all cases.

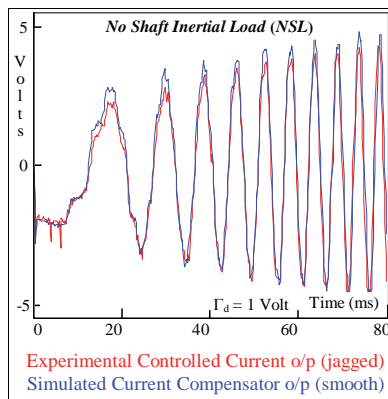


Fig. 31. Current compensator o/p V_{ca}

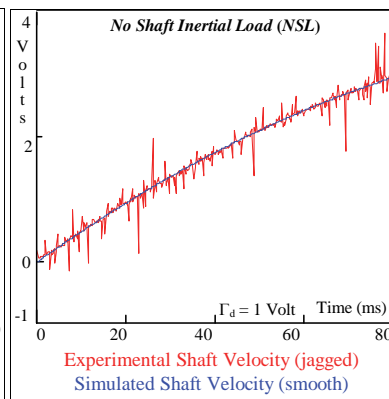


Fig. 32. RDC-rotor shaft velocity V_{ω}

Both the simulated current transients $i_{da}(kT)$ and $i_{fa}(kT)$ exhibit the characteristics of a frequency modulated sinusoid with fixed amplitude and swept frequency due to the exponential buildup of motor shaft speed during the acceleration phase. This can be visualized from the amplitude spectrum shown in Figure 33, for the extended filtered feedback current displayed in Figure 34, which appears constant over the electrical frequency band of 286 Hz corresponding to the swept motor speed range from standstill to 3000 RPM. These simulated waveforms provide an excellent fit in terms of frequency and phase coherence with test data when correlated. The measure of fit in this instance is expressed by the trace response correlation coefficients, listed in Table III, as

$$\rho = \frac{\text{Cov}(I_{xa}, i_{xa})}{\sqrt{V(I_{xa})V(i_{xa})}} \tag{LXXXIX}$$

where $\text{Cov}(I_{xa}, i_{xa})$, $V(I_{xa})$, and $V(i_{xa})$ are the covariance and respective variance measures.

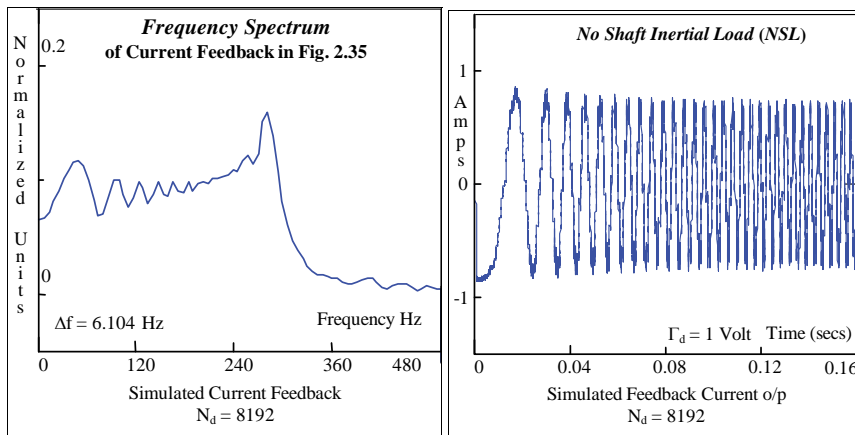


Fig. 33. Spectrum of motor FC $I_{fa}(\omega)$

Fig. 34. BLMD model FC I_{fa}

Furthermore the accuracy of fit of the simulated traces consisting of the shaft velocity and current controller output with experimental step response test data, as indicated by the correlation coefficients in Table III, confirms model integrity. The fidelity and coherence of BLMD model trace simulation, when compared with drive experimental test data, is also established for known inertial shaft loads (Guinee, 1998, 1999) which further substantiates model accuracy and confidence. A number of BLMD transient waveform simulations, based on established model accuracy and confidence, at strategic internal nodes provide insight into and confirmation of motor drive operation during the acceleration phase. The filtered feedback current from each phase of the motor winding to the compensators in the three phase current control loop is illustrated in Figure 35. These waveforms show a reduction in the period of oscillation, accompanied by a very slight decrease in amplitude due to the impact of back emf reaction and machine impedance effects, as expected with an increase in shaft speed.

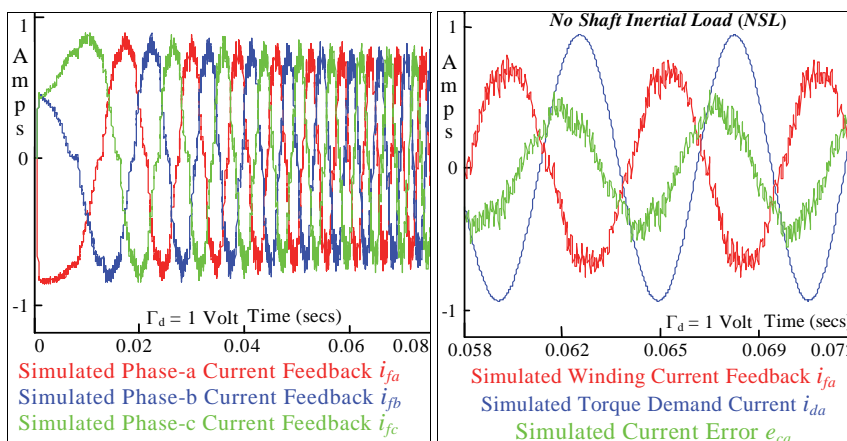


Fig. 35. BLMD 3Φ FC simulation I_{fj}

Fig. 36. Current controller inputs

A snapshot in time shows the relative amplitude and phase differences between the simulated phase-a i/p current waveforms i_{fa} and i_{dar} in the form of the resultant comparison signal error v_{ca} to the current controller, in Figure 36 during motor speed-up. This error is primarily due to the increasing phase difference between the torque command current i_{dar} issued to each phase of the motor winding through the current controlled inverter response voltage v_{asr} and the actual phase current flow i_{as} as a result of the stator winding impedance angle increase in (LXXXIV) with motor speed.

The simulated complementary turn-on signals issued to the basedrive from the RC delay ‘lockout’ circuit are shown in Figure 37 over a number of PWM switching periods along with the threshold voltage which determines the basedrive trigger timing. The corresponding PWM inverter controlled 3Φ output pole voltages v_{jg} fed to the stator winding i/p, including the neutral potential v_{sg} derived from (LVIII), are shown in Figure 38 over several switching intervals. These simulated binary level width-modulated pulses, which have a voltage excursion from ground potential to the dc busbar high tension level U_{dr} , result in the six step phase voltage waveform v_{as} illustrated in Figure 39.

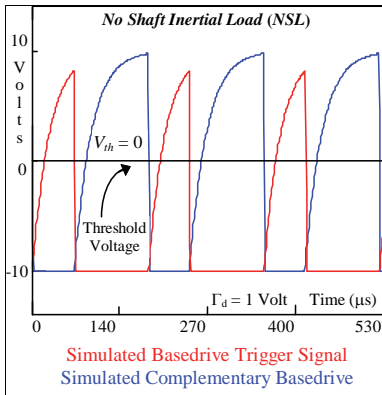


Fig. 37. Basedrive command signals

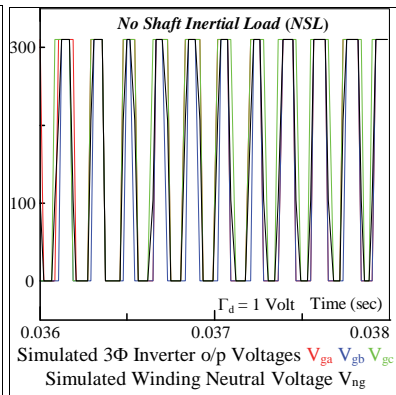


Fig. 38. PWM inverter o/p voltage

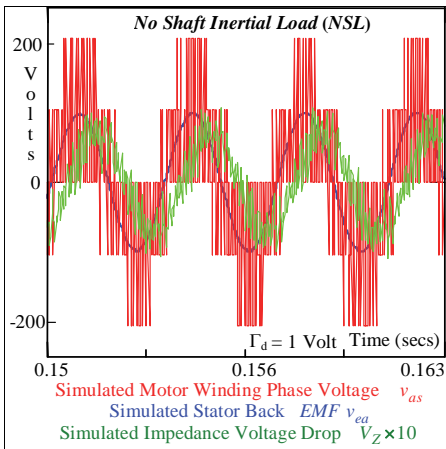


Fig. 39. Stator phase voltages

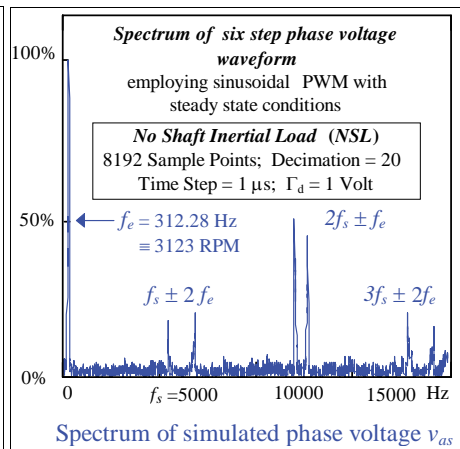


Fig. 40. Spectrum of phase voltage v_{as}

The stator back EMF phase voltage v_{ea} together with the winding impedance voltage drop v_z , which is magnified tenfold for display reasons, are shown in Figure 39 for comparison purposes as the motor rotational speed (~ 3120 rpm) approaches the maximum steady state nominal value of 4000 rpm. The motor impedance voltage $|V_z|$ drop, which is mainly inductive at this speed and determined from

$$V_z = i_{js} \cdot \sqrt{r_s^2 + (p\omega_r L_s)^2} e^{j\phi_z} = |Z| e^{j\phi_z} \cdot i_{js} \tag{XC}$$

with impedance angle ϕ_z as per (LXXXIV), is negligible compared to the reaction EMF as the current required to sustain frictional torque in (LXXXVI) is minimal.

The normalized spectrum of the six step phase voltage, which has a sharp line structure indicative of steady state motor operation close to rated speed, is displayed in Figure 40. This amplitude spectrum, which is the characteristic signature of sub-harmonic PWM inverter operation (Murphy et al, 1998), consists of the fundamental machine electrical frequency f_e (~ 312 Hz) and side frequency component pairs ($kf_s \pm nf_e$) associated with pulse generation about the triangular carrier switching harmonics kf_s . The side frequency distribution contains even order pairs symmetrically disposed about odd carrier harmonics and odd order pairs about even harmonics with significant amplitudes dependent on the index of modulation m_f in (LIII). These extraneous component contributions are located well outside the machine winding passband, which has a 3dB cutoff frequency f_c determined from the stator electrical time constant $\tau_e = L_s/r_s$ (~ 2.6 ms) in Table I as

$$f_c = (2\pi\tau_e)^{-1} \approx 61.2\text{Hz}, \tag{XCI}$$

by choice of the carrier switching frequency f_s (~ 5 kHz). These distortion components are thus heavily suppressed through attenuation by the stator winding inductance.

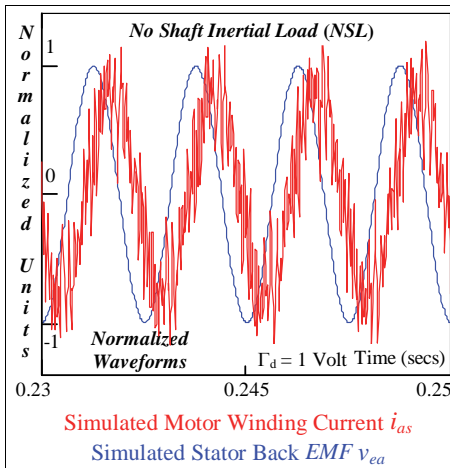


Fig. 41. Phase current & back EMF

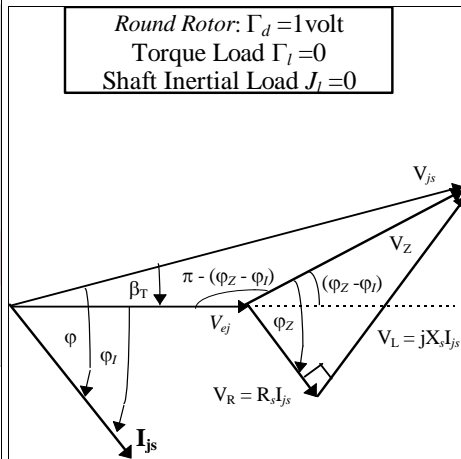


Fig. 42. Stator phasor diagram

The winding currents lag the reaction EMF as shown in Figure 41 by the internal power factor angle $\phi_l \approx 66.6^\circ$, obtained from statistical averaging of the estimated crossover

instants, near rated motor speed. This lag, which can be calculated as 65.7° from the average mechanical power delivered using the rms quantities in Table IV and Figure 42 with

$$P_m = 3V_{ej}I_{js} \cos \varphi_1 , \tag{XCII}$$

differs from the machine impedance angle obtained from the BLMD model simulation shown in Figure 43 as $\varphi_z \approx 78^\circ$ using (LXXXIV) near rated motor speed.

The stator winding voltage and current phasors including relevant phase angles are illustrated in Figure 42 at near rated motor speed for zero torque load conditions with magnitude estimates listed in Table IV. The actual and internal power factor angles, φ and φ_1 respectively, are almost identical for zero torque load conditions resulting in negligible load angle β_T . This can be established by geometrically determining from Figure 42 the voltage phasor V_{js} applied to the motor winding as

$$V_{js} = \sqrt{V_{ej}^2 + V_z^2 + 2V_{ej}V_z \cos(\varphi_z - \varphi_1)} . \tag{XCIII}$$

Evaluation Period: $0.2s \leq t \leq 0.24s$	Resistance Voltage $V_R = R_s I_{js} = 1.14v$	Phase Voltage (XCIII): $V_{js} = 81.3v$
Mech-Power (LXXXVIII): $P_m = 141.2 \text{ w}$	Reactance Voltage $V_L = jX_s I_{js} = j5.9v$	Impedance Angle (LXXXIV): $\varphi_z = 79.1^\circ$
Shaft Velocity: $\omega_r = 334 \text{ rad.sec}^{-1}$	RMS Impedance Voltage (Fig. 39): $V_z = 6v$	Int-Pow-Fac Angle (XCII): $\varphi_1 = 65.7^\circ$
RMS Current (Fig. 34): $I_{as} = 1.5A$	RMS Reaction EMF (Fig. 39): $V_{ej} = 75.3v$	Load Angle (XCV): $\beta_T = 1.06^\circ$
Estimated φ_1 (Fig. 40) $\varphi_1 = 66.55^\circ$	RMS Phase Voltage (Fig. 39) $V_{js} = 78v$	Pow-Factor Angle $\varphi = 66.8^\circ$

Table IV. Evaluation of phasor magnitudes from steady state conditions in figure 42

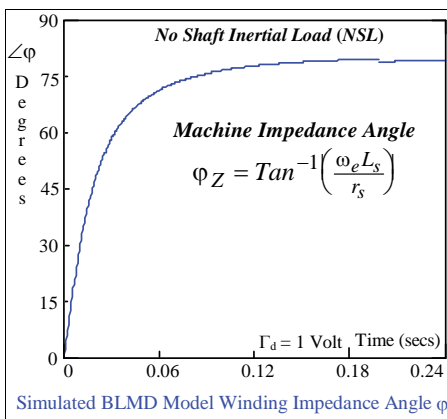


Fig. 43. Motor impedance angle

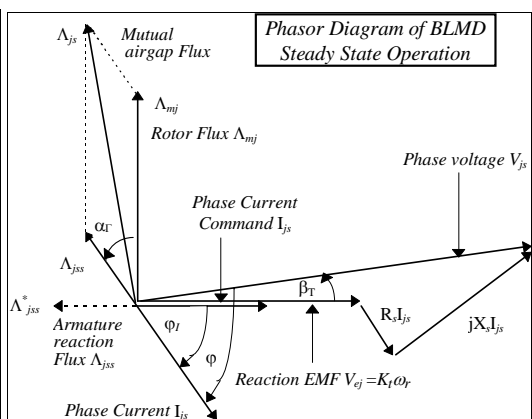


Fig. 44. Phasor diagram of brushless motor

This can then be used in the evaluation of the load angle β_T using

$$\frac{V_z}{\sin \beta_T} = \frac{V_{js}}{\sin\{\pi - (\varphi_z - \varphi_1)\}} \text{ as} \tag{XCIV}$$

$$\beta_T = \sin^{-1} \left\{ \frac{V_z}{V_{js}} \sin(\varphi_z - \varphi_1) \right\} \tag{XCV}$$

with $\beta_T = 1.06^\circ$ upon substitution of the phasor quantities in Table IV. When a finite load torque is applied to the BLMD shaft a noticeable difference develops between the actual and internal power factor angles with an increase in load angle β_T , appropriate to the value of load power necessary to sustain the applied load torque and friction losses, as the motor approaches rated angular velocity ω_{rmax} . In the development of the torque expression in (XLII), which can be re-expressed as

$$\Gamma_e(I_s, \theta_r) = K_e \sum_{j=1}^3 \cos\left(p\theta_r - \frac{2(j-1)\pi}{3}\right) i_{js} = \left(\frac{1}{\theta_r}\right) \sum_{j=1}^3 v_{ej} \cdot i_{js} \tag{XCVI}$$

using (XXIV) it is assumed that the stator winding back EMF v_{ej} is in phase with the forced stator current i_{js} , in response to the equal magnitude current demand i_{dj} from shaft sensor position information, for maximum torque production via the applied and electronically commutated stator terminal voltage v_{sj} . This assumption, however, is not accurate in that a phase lag equal to the power factor angle φ develops with shaft velocity between the injected current I_{js} and voltage V_{js} phasors as shown in Figure 44. During normal motor operation current commutation is used in an attempt to maintain a virtual armature flux phasor Λ_{jss}^* in quadrature with the rotor flux, in accordance with fixed current demand, for maximum motor torque production. As the motor reaches rated speed, for zero shaft load torque conditions, the motor impedance angle φ_z in Figure 42 increases along with the back EMF V_{ej} . The cumulative effect of increased impedance voltage V_z with V_{ej} result in further current lag by the angle φ in order to comply with fixed torque current demand via the applied stator phase voltage V_{js} .

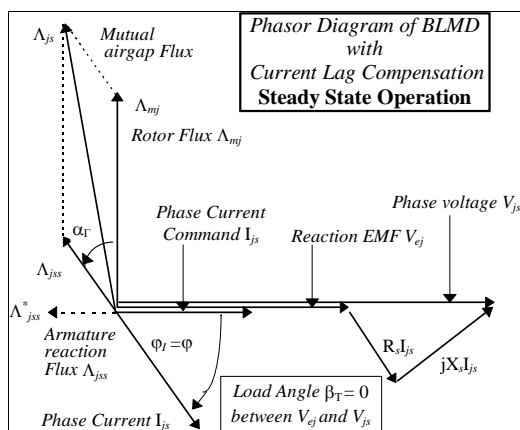


Fig. 45. Current lag compensation

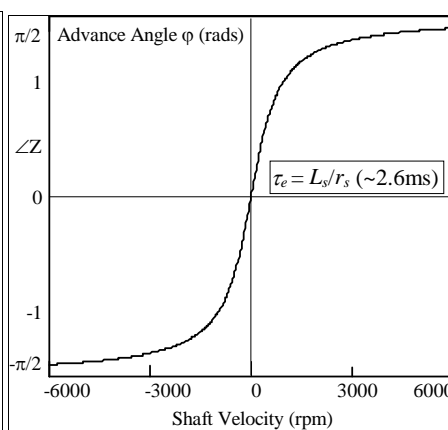


Fig. 46. Commutation phase lead

Consequently the applied torque Γ_e decreases with increased angular displacement ϕ_1 between the inverter controlled stator current flow and EMF phasors in accordance with (XCII) as

$$\Gamma_e = \frac{P_m}{\omega_r} = 3K_t I_{js} \cos \phi_1 . \tag{XCVII}$$

The internal power factor angle adjusts towards 90° to reduce the torque angle α_T in (XLVIII) with reaction EMF increase in compliance with load torque requirements as shown in Figure 44. The increase of current lag ϕ , with impedance angle ϕ_z due to motor speed, can be compensated for with power factor correction by electronically advancing the current command phase angle in accordance with (LXXXIV), in the current commutator circuit of Figures 1 and 28, as

$$p\theta_r - 2(j-1)\frac{\pi}{3} \rightarrow (p\theta_r + \phi_z) - 2(j-1)\frac{\pi}{3} \tag{XCVIII}$$

In this scheme the load angle β_T between the terminal voltage V_{js} and back EMF phasors is forced to zero with inverter controlled winding voltages that are collinear with the current demand I_{ds} phasors as shown in Figure 45. The commutation phase lead angle required to nullify the torque reduction effects at different motor speeds is displayed in Figure 46.

The motor airgap torque Γ_e displayed in Figure 47, which utilizes expression (XLII) during BLMD model simulation, appears to be numerically ‘noisy’. This apparent ‘noisiness’ result from the carrier harmonic contribution as high frequency ripple, due to PWM inverter operation, superimposed on the stator winding current flow. This sawtooth ripple manifestation is transferred via stator winding current injection to the magnetic coupling in the EM torque generation process. This ripple is primarily due to the nonlinear pulse nature of the delayed PWM process manifested as superimposed extraneous phase current harmonics, shown in Figure 48 as phase current ripple, mixing with the fundamental phase reference $\cos[p\theta_r - 2(j-1)\frac{\pi}{3}]$ in the torque product expression (XLIII). The smoothed torque characteristic is also shown in Figure 47 for measurement clarity and reference purposes with ‘noisy’ data filtering identical to the torque demand i/p filter employed.

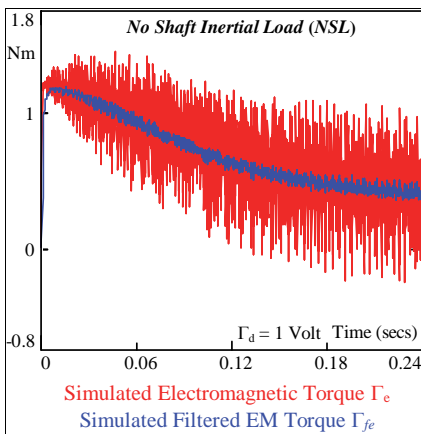


Fig. 47. Simulated airgap torque Γ_e

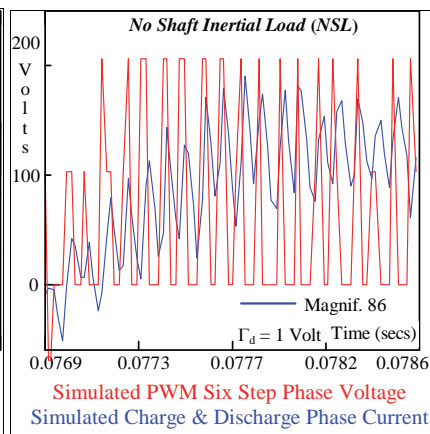


Fig. 48. Phase ripple current

The rotor inertia J_m and damping B_m , inherent in the BLMD system, has a smoothing effect on the generated electromagnetic torque Γ_e by virtue of the integrating action of the equivalent low pass filter characteristics of the motor dynamics given by

$$\frac{\omega_r}{\Gamma_e}(s) = \frac{1}{J_ms + B_m} \tag{XCIX}$$

with a 3dB cutoff radiancy based on parameters from Table II of

$$w_m = B_m / J_m \approx 7 \text{ rad.sec}^{-1} \tag{C}$$

This results in the smooth mechanical motion illustrated as the simulated motor shaft velocity in Fig. 49. As the motor reaches rated speed the generated torque decreases to that necessary in (LXXXVI) to sustain motion with frictional torque retardation. The simulated power transfer and the filtered version derived from the developed torque characteristics, depicted in Figure 47 using expression (XLVI), are shown in Figure 50. The net motive power required under steady state conditions, at a motor speed of $\omega_r \sim 310 \text{ rad.sec}^{-1}$, to overhaul mechanical losses is $P_m \sim 182 \text{ watts}$ which correlates reasonably well with the friction power estimate of $P_f \sim 200 \text{ watts}$ obtained from Figure 27.

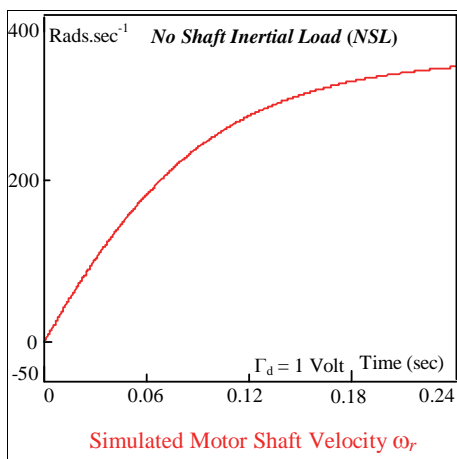


Fig. 49. Simulated shaft velocity

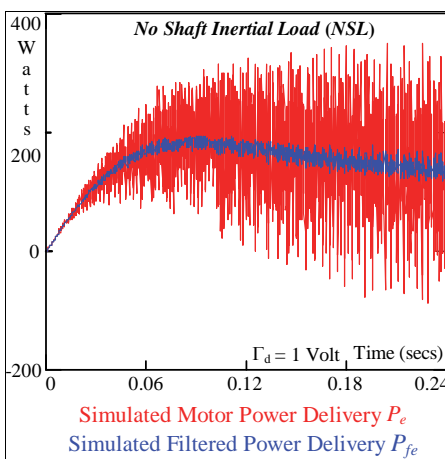


Fig. 50. Mechanical power delivery

3.4 Effects of PWM inverter delay

The influence of inverter delay on both motor torque and speed reduction can be visualized in Figures 51 and 52. Since torque command current magnitude is encoded as a modulated pulse duration τ_m during the PWM process an inverter dead zone is equivalent to a drop in voltage transport to the motor stator windings. The resultant decrease in motor winding current amplitude can be estimated, via (LII) with the aid of Figures 13 and 14, from consideration of the inverter blanking period required for transistor bridge protection with a consequent loss of mechanical torque delivery expressed by (XLV). When current flow i_{js} is positive the modulated pulse ON time of the appropriate power transistor T_{J+} , in the absence of inverter blanking with winding connection to the dc busbar U_d , is given by

$$t_{on} = \tau_m = (1 + m_f) \frac{T_s}{2} \tag{CI}$$

which also corresponds to the OFF time of T_{J-} . When a dead zone is introduced into inverter operation, during which forced winding current injection is impeded but with flywheel conduction maintained through diode D_j in Figure 15 at ground potential, the resulting switch-on time for T_{J+} is given by

$$t_{on}^* = (\tau_m - \delta) = (1 + m_f) \frac{T_s}{2} - \delta \tag{CII}$$

Similar switch-on time expressions hold for T_{J-} operation during negative current flow. The effect of inverter delay can be seen in the BLMD current feedback simulation as crossover distortion in Fig. 53 when contrasted with the FC trace without delay.

The relative percentage current flow with dead time is determined by the ratio of the switch-on times in (CI) and (CII) as

$$t_{on}^*/t_{on} = \left[1 - \frac{2\delta}{(1+m_f)T_s} \right] 100\% \tag{CIII}$$

which for a unit torque demand input with $MI = 0.145$ ($= 1/6.9$), $T_s = 176\mu s$ and $\delta = 19.6\mu s$ in Figure 53 is estimated as 80.5%. The percentage ratio of the corresponding rms feedback currents, with and without delay respectively in Figure 53 over the extended time span of 0.24 secs, is 78.5% ($=1.555/1.981$) which is almost identical to that from pulse time considerations. The resultant torque ratio from Figure 51 is also approximately 80%, as it is proportional to the current ratio, in the settled region which corresponds to the torque necessary to overhaul frictional effects. Motor shaft speed exhibits a similar variation in Figure 52, since it is proportional to the time integral of the torque, with delay of about 82.5%.

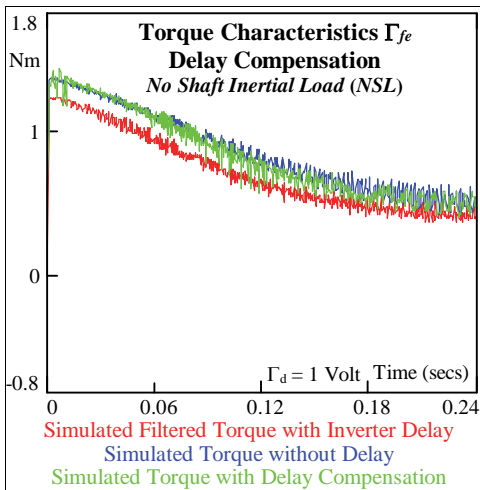


Fig. 51. Torque reduction with lag

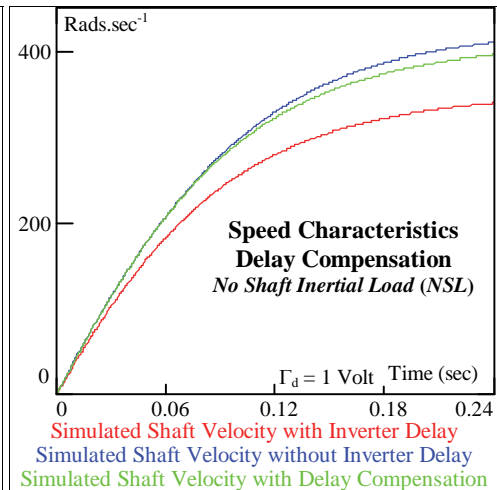


Fig. 52. Motor speed compensation

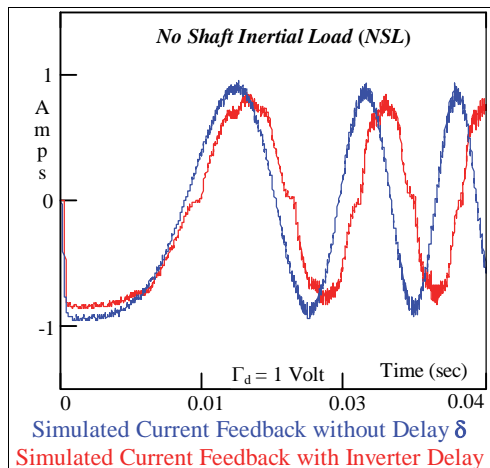


Fig. 53. Effect of inverter lag on FC

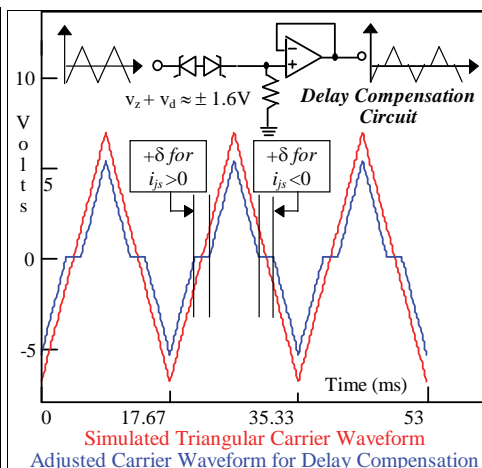


Fig. 54. Inverter delay compensation

3.5 Novel PWM Inverter dead-time compensation

Timing counter circuits with optocoupler isolation (Murai et al, 1985, 1992) have been used for delay correction in each phase during PWM operation of induction motors. A novel and simpler solution is proposed here for simultaneous delay compensation in all three phases through amplitude adjustment of the triangular dither waveform. The technique relies on the simple expedient of additional symmetrical double edge pulse widening during PWM, via the signal magnitude comparison with a reduced carrier amplitude contribution, to counterbalance the effects of inverter lag. The additional modulation index Δm_f required for increased pulse duration using (CI) to nullify the effect of inverter delay in (CII) is

$$\Delta m_f = \frac{\Delta V}{V_{tri}} = \frac{2\delta}{T_s} \approx 0.225 \tag{CIV}$$

which translates into an amplitude reduction of the positive going excursion of the triangular carrier waveform as

$$\Delta V = \Delta m_f V_{tri} = (0.225) \cdot (6.9) = 1.553. \tag{CV}$$

A similar pulse elongation time is associated, during periods of negative winding current flow, with the negative carrier amplitude reduction. The implementation of the requisite bipolar amplitude decrease is facilitated by the back-to-back zener diode combination, with buffer amplifier isolation as shown in Figure 54, which imparts a cumulative voltage clipping V_{CL} of

$$V_{CL} = V_z + V_d = \pm 1.6V \tag{CVI}$$

in the neighborhood of the dither signal $V_{tri}(t)$ polarity changeover where V_z is the zener voltage and V_d is the forward diode voltage drop. The compensatory effect of added pulse time on the torque and speed curves with inverter delay operation is shown in Figures 51 and 52 respectively. These characteristics are almost congruent with model simulations

linked with zero inverter lag over most of the motor speed range. The discrepancy at high speeds, although small, is associated with the lead time distribution about the modulated pulse double edge rather than at the leading edge where it should be concentrated to counteract the effects of inverter blanking. The quality of the lag compensation method can be better gauged from the phase and frequency coherency of the BLMD model FC responses illustrated in Figure 55 which are well correlated with a goodness-of-fit correlation coefficient of 91.7% using (LXXXIX).

4. Conclusions

A detailed and accurate reference model, based on physical principles, of a typical embedded BLMD system used for EV propulsion and high performance motive power industrial applications has been presented for the express purpose of computer aided design and simulation of EV propulsion systems where performance prediction and evaluation are a necessity before fabrication. Model fidelity is confirmed by extensive numerical simulation with particular emphasis at critical internal observation nodes when contrasted with measured data from a high performance PM drive system. Model validation for identification purposes is provided by frequency and phase coherence of simulated data with step response transient current feedback test data possessing FM attributes. A novel and effective delay compensation solution, based on carrier voltage level adjustment for multi-phase operation, is provided to counterbalance the effect of inverter blanking in torque reduction which is substantiated by BLMD model simulation.

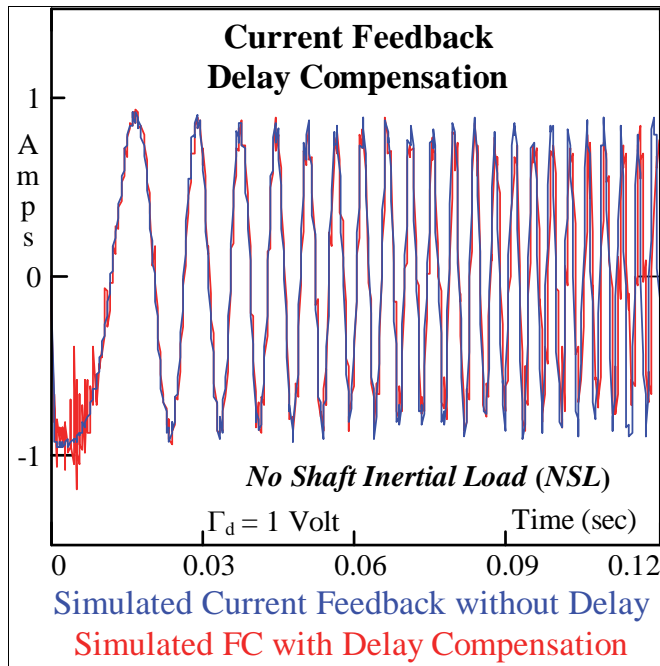


Fig. 55. FC delay compensation

5. Acknowledgment

The author wishes to acknowledge

- i Eolas - The Irish Science and Technology Agency - for research funding.
- ii Moog Ireland Ltd for brushless motor drive equipment for research purposes.

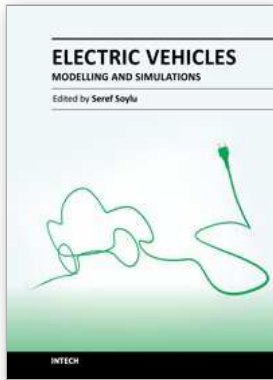
6. References

- Adams, R.D. & Fox, R.S.; (1975). Several Modulation Techniques for a Pulsewidth Modulated Inverter, *IEEE Trans. on Industry Applications*, Vol. IA-8, No. 5.
- Asada, H. & Youcef-Toumi, K.; (1987). *Direct-Drive Robots Theory and Practice*, MIT Press. Camb., Mass.
- Astrom, K.J. & Hagglund, T.; (1988). *Automatic Tuning of PID Controllers*, Instrument Society Of America, ISBN 1-55617-081-5.
- Astrom, K.J. & Wittenmark, B.; (1989). *Adaptive Control*, Addison-Wesley.
- Basak, A.; (1996) *Permanent Magnet DC linear Motors*, Clarendon Press, Oxford
- Boldea, I.; (1996). *Reluctance Synchronous Machines and Drives*, Oxford Science Publications, OUP
- Brickwedde, A.; (1985). Microprocessor-Based Adaptive Speed and Position Control for Electrical Drives, *IEEE Trans. on IAS*, Vol. IA-21, No. 5, pp1154-1161.
- Bulmer, M.G.; (1979). *Principles of Statistics*, Dover Publications Inc., New York.
- Chalam, V.V.; (1987). *Adaptive Control Systems: Techniques and Applications*, Marcel Dekker.
- Crangle, J.; (1991). *Solid State Magnetism*, Edward Arnold Publishers.
- Crowder, R.M.; (1995). *Electric Drives and their Controls*, Clarendon Press, Oxford.
- Dawson, D.M; Hu, J & Burg, T.C.; (1998). *Nonlinear Control of Electric Machinery*, Marcel Dekker.
- Demerdash, N.A; Nehl T.W. & Maslowski E.; (1980). Dynamic modelling of brushless dc motors in electric propulsion and electromechanical actuation by digital techniques, *IEEE/IAS Conf. Rec.* CH1575-0/80/0000-0570.
- Demerdash, N.A. & Nehl, T.W.; (1980). Dynamic Modelling of Brushless dc Motors for Aerospace Applications", *IEEE Trans. On Aerospace and Electronic Systems*, Vol. AES-16, No. 6.
- Dodson, R.C., Evans, P.D., Tabatabaei, H. & Harley, S.C.; (1990). Compensating for dead time degradation of PWM inverter waveforms, *IEE Proc.*, Vol. 137, Pt. B, No. 2.
- Dohmeki, H. & Nasu, M.; (1985). Development of a Brushless DC Motor for Incremental Motion Systems", *Proc. 14th IMCSD annual Symp.*
- Dote, Y.; (1990). *Servo Motor and Motion Control using Digital Signal Processors*, PHI.
- Electrocraft Corp; (1980). *DC Motors, Speed Control, Servo Systems*, 5th Edition.
- El-Sharkawi, M.A. & Huang, C.H.; (1989). Variable Structure Tracking of Motor for High Performance Applications, *IEEE Trans. on Energy Conv.*, Vol. 4, No.4.
- El-Sharkawi, M.A. & Weerasooriya, S.; (1990). Development and Implementation on Self-Tuning Tracking Controllers for DC Motors, *IEEE Trans. on Energy Conv.*, Vol. 5, No. 1.
- EL_Sharkawi, M.A. ; (1991). *Advanced control techniques for High Performance Electric Drives, Control and Dynamic Systems*, Academic Press, pp. 59-130, Vol 44, 1991.

- El-Sharkawi, M.A., El-Samahy, A.A. & El-Sayed, M.L.; (1994). High Performance Drive of DC Brushless Motors Using Neural Network", *IEEE Trans. on Energy Conversion*, Vol.9.
- Emadi, A.; Ehsani, M. & Miller, J. M. (2003). *Vehicular Electric Power Systems: Land, Sea, Air, and Space Vehicles*, CRC Press.
- Evans, P.D. & Close, P.R.; (1987). Harmonic Distortion in PWM inverter output Waveforms", *IEE Proc.*, Vol 134, Pt. B, No. 4.
- Franklin, G.F. & Powell, J.D.; (1980). *Digital Control Of Dynamic Systems*, Addison Wesley.
- Friedrich, G. & Kant, M.; (1998). Choice of drives for electric vehicles: a comparison between two permanent magnet AC machines, *IEE Proc.-Elec. Power Appl.*, Vol. 145, No. 3.
- Grant, D.A. & Seidner, R.; (1981). Ratio Changing in pulse-width-modulated inverters", *IEE Proc.*, Vol. 128, Pt. B, No. 5.
- Grant, D.A., Houldsworth, J.A. & Lower, K.N.; (1983). A New High-Quality PWM AC Drive", *IEEE Trans. on Industry Applications*, Vol IA-19, No. 2.
- Guinee, R.A. & Lyden, C.; (1998). A Novel Single Fourier Series Technique for the Simulation and Analysis of Asynchronous Pulse Width Modulation, *IEEE 13th Annual Applied Power Electronics Conference and Exposition, APEC'98*, Anaheim, California.
- Guinee, R.A. & Lyden, C.; (1998). An Improved Simulation Model of a Brushless DC Motor Drive System for Industrial Applications, *IEEE 9th Mediterranean Electrotechnical Conference, MELECON'98*, Tel-Aviv, ISRAEL.
- Guinee, R.A. & Lyden, C.; (1998). Accurate Modelling and Simulation of a High Performance Brushless DC Motor Drive System for Industrial Applications, *Proc. of the IASTED International Conference Applied Modelling and Simulation*, Honolulu, Hawaii.
- Guinee, R.A. & Lyden, C.; (1999). Accurate Modelling And Simulation Of A DC Brushless Motor Drive System For High Performance Industrial Applications, *IEEE ISCAS'99 - IEEE International Symposium on Circuits and Systems*, May/June 1999, Orlando, Florida
- Guinee, R.A. & Lyden, C.; (1999). Parameter Identification of a Brushless Motor Drive System using a Modified Version of the Fast Simulated Diffusion Algorithm, *Proc. of American Control Conference - IEEE ACC-1999*, San Diego, pp.3467-3471.
- Guinee, R.A. & Lyden, C.; (1999). Accurate Modelling and Simulation of a High Performance Permanent Magnet Adjustable Speed Drive System for Embedded Systems", *8th European Conference on Power Electronics and Applications - EPE'99*, Lausanne, Switzerland.
- Guinee, R.A. & Lyden, C.; (2000) A Novel Application of the Fast Simulated Diffusion Optimization Technique for Brushless Motor Parameter Extraction, *UKACC International Conference on Control*, Cambridge Univ.
- Guinee, R.A. & Lyden, C.; (2001), Motor Parameter Identification using Response Surface Simulation and Analysis, *Proc. of American Control Conference, ACC-2001*, VA, USA.
- Guinee, R.A.; (2003). *Modelling, Simulation, and Parameter Identification of a Permanent Magnet Brushless Motor Drive System*, Ph. D. Thesis, NUI - University College Cork.
- Guinee, R.A.; (2005). Dead Time Compensation in PWM Inverter Transistor operation for Improved Brushless Motor Drive System Performance, *Universities Power Engineering Conference, UPEC 2005*, University College Cork.

- Guinee, R.A.; (2009). *A Novel Dead Time Compensation Circuit for Improved PWM Inverter Operation in Brushless Motor Drive Systems for Electric Vehicle*, 5th IEEE Vehicle Power and Propulsion Conference (VPPC'09), Dearborn, MI 48128, USA
- Hang, C.C. & Sin, K.K.; (1991). "A Comparative Performance Study of PID Auto-Tuners", *IEEE Control Systems*, 0272-1708/91/0800-004.
- Hendershot, J.R. & Miller, T.J.E.; (1994). *Design of Brushless Permanent-Magnet Motors*, Magna Physics Publishing and Clarendon Press, Oxford.
- Jahns, T.M.; (1984). "Torque Production in Permanent Magnet Synchronous Motor Drives with Rectangular Current Excitation", *IEEE Trans. on Industry Applications*, Vol IA-20, No. 4.
- Johansson, R.; (1993). *System Modelling and Identification*, Prentice Hall.
- Kuo, B.C. & Tal, J.; (1978). *Incremental Motion Control Systems: DC Motors and Control Systems*, SRL Publ. Co., illinois.
- Kraus, H.L., Bostian C.W. & Raab, F.H.; (1980). *Solid State Radio Engineering*, J. Wiley & Sons.
- Krause, P.C.; (1986). *Analysis of Electric Machinery*, McGraw-Hill
- Krause, P.C. & Wasynczuk, O.; (1989) *Electromechanical Motion Devices*, McGraw-Hill.
- Kreyszig, E.; (1972). *Advanced Engineering Mathematics*, J. Wiley & Sons.
- Leu, M.C., Liu S. & Zhang, H.; (1989). "Modelling, Analysis and Simulation of Brushless DC Drive System", *Winter Annual Meeting of ASME*, 89-WA/DSC-1, San Francisco.
- Ljung, L.; (1987). *System identification: Theory For The User*, PHI.
- Ljung, L.; (1991). "Issues in System Identification", *IEEE Control Systems*, 0272-1708/91/0100-0025.
- Ljung, L.; (1992). "A Discussion Of Model Accuracy In System Identification", *International Journal Of Adaptive Control and Signal Processing*, Vol.6, pp.161-171, J. Wiley & Sons.
- Matsch, L.W.; (1972). *Electromagnetic and Electromechanical Machines*, Intext Educational Publishers.
- Meshkat, S.; (1985). "A new Microprocessor Based Brushless Servo Amplifier for Optimum Current Vector Control", *Proc. 13th IMCSD ann. symp.*, pp 19-24.
- Miller, J.; (2010). *Propulsion Systems for Hybrid Vehicles*, IET, Renewable Energy, 2nd Edition.
- Mohan, N.; (1998). "Understanding Basics of Adjustable Speed and Vector-Controlled Induction and Synchronous Motor Drives", Seminar S1, *APEC'98 - Applied Power Electronics Conference and Exposition*, Anaheim, California.
- Moog GmbH; (1988). *Moog Brushless Technology:Brushless Servodrives User Manual*, D310.01.03 En/De/It 01.88, Moog GmbH, D-7030 Böblingen, Germany.
- Moog GmbH; (1989). *Moog Brushless Technology User Manual:D31X-XXX Motors,T158-01X Controllers,T157-001 Power Supply*, , D-7030 Böblingen.
- Murai, Y., Watanabe, T. & Iwasaki, H.; (1985). "Waveform Distortion And Correction Circuit For PWM Inverters With Switching Lag Times", *IEEE IAS Annual Meeting*, Toronto, pp436-441, *IEEE CH2207-9/85/0000-0436*.
- Murai, Y., Riyanto, A., Nakamura, H. & Matsui, K.; (1992). "PWM Strategy for High Frequency Carrier Inverters Eliminating Current-Clamps during Switching Dead-Time", 0-7803-0634-1/92, Houston, USA.
- Murphy, J.M. & Turnbull, F.G.; (1989). *Power Electronic Control of AC Motors*, Pergammon Press.
- Murugesan, S.; (1981). "An Overview of Electric Motors for Space Applications", *IEEE Trans. on Ind. Elec. and Control Inst.*, Vol. IECI-28, No. 4.

- Naitoh, H. & Tadakuma, S.; (1987). "Microprocessor-Based Adjustable-Speed DC Motor Drives using Model Reference Adaptive Control", *IEEE Trans. on IAS*, Vol. IA-23, No. 2, pp 313-318.
- Noodleman, S.; (1975). A New Type DC Motor, *IEEE Trans. on Ind. Appl.*, Vol. IA-11, No. 3.
- Persson, E.K. & Buric, M.; (1976). Mathematical Modelling and Simulation of High Performance Brushless DC Motors, *IMCSD 4th annual symp.*
- Pollack, J.J.; (1972). Advanced Pulsewidth Modulated Inverter techniques, *IEEE Trans. on Industry Applications*, Vol. IA-8, No. 2.
- Press, W.H., Flannery, B.F., Teukolsky, S.A. & Vetterling, W.T.; (1990). *Numerical Recipes in C*, CUP.
- Soderstrom, T. & Stoica, P.: (1989), *System Identification*, Prentice Hall Internat.
- Spooner, E. & Williamson, A.C.; (1996). Direct coupled, permanent magnet generators for wind turbine applications, *IEE Proc.-Electr. Power Appl.*, Vol. 143, No. 1.
- Tal, J.; (1976). Design and Analysis of Pulsewidth-Modulated Amplifiers for DC Servo Systems, *IEEE Trans. on Industrial Electronics and Control Instrumentation*, Vol IECI 23, No.1.
- Tomasek, J.; (1979). Brushless Servo Motor - Amplifier Optimization, *Proc. of 8th Ann. Symp. of Incremental Motion Control Systems and Devices*, Univ. of Illinois.
- Tomasek, J.; (1983). Analysis of Torque-Speed Performance Limits in Brushless DC Servo Systems, *Proc. of 12th Ann. Symp. of Incremental Motion Control Systems and Devices*, Illinois Univ
- Tomasek, J.; (1986). "Basic Performance Specifications and Ratings for Sine-Wave Brushless Servo Systems, *Proc. of 15th Ann. Symp. of Incremental Motion Control Systems and Devices*.
- Vas, P; (1998). *Sensorless Vector and Direct Torque Control*, Oxford Univ.
- Weerasooriya, S. & El-Sharkawi, M.A.; (1989). Adaptive Tracking Control for High Performance DC Drives, *IEEE Trans. on Energy Conv.*, Vol. 4, No. 3.



Electric Vehicles - Modelling and Simulations

Edited by Dr. Seref Soylu

ISBN 978-953-307-477-1

Hard cover, 466 pages

Publisher InTech

Published online 12, September, 2011

Published in print edition September, 2011

In this book, modeling and simulation of electric vehicles and their components have been emphasized chapter by chapter with valuable contribution of many researchers who work on both technical and regulatory sides of the field. Mathematical models for electrical vehicles and their components were introduced and merged together to make this book a guide for industry, academia and policy makers.

How to reference

In order to correctly reference this scholarly work, feel free to copy and paste the following:

Richard A. Guinee (2011). Mathematical Modelling and Simulation of a PWM Inverter Controlled Brushless Motor Drive System from Physical Principles for Electric Vehicle Propulsion Applications, *Electric Vehicles - Modelling and Simulations*, Dr. Seref Soylu (Ed.), ISBN: 978-953-307-477-1, InTech, Available from: <http://www.intechopen.com/books/electric-vehicles-modelling-and-simulations/mathematical-modelling-and-simulation-of-a-pwm-inverter-controlled-brushless-motor-drive-system-from>

INTECH

open science | open minds

InTech Europe

University Campus STeP Ri
Slavka Krautzeka 83/A
51000 Rijeka, Croatia
Phone: +385 (51) 770 447
Fax: +385 (51) 686 166
www.intechopen.com

InTech China

Unit 405, Office Block, Hotel Equatorial Shanghai
No.65, Yan An Road (West), Shanghai, 200040, China
中国上海市延安西路65号上海国际贵都大饭店办公楼405单元
Phone: +86-21-62489820
Fax: +86-21-62489821

© 2011 The Author(s). Licensee IntechOpen. This chapter is distributed under the terms of the [Creative Commons Attribution-NonCommercial-ShareAlike-3.0 License](#), which permits use, distribution and reproduction for non-commercial purposes, provided the original is properly cited and derivative works building on this content are distributed under the same license.